S. SUNJAI NAKSHATHARAN

Electromechanical modelling and control of ionic electroactive polymer actuators

DISSERTATIONES TECHNOLOGIAE UNIVERSITATIS TARTUENSIS

54

S. SUNJAI NAKSHATHARAN

Electromechanical modelling and control of ionic electroactive polymer actuators

Institute of Technology, Faculty of Science and Technology, University of Tartu, Estonia

This dissertation was accepted for the commencement of the degree of Doctor of Philosophy in Physical Engineering on June 3rd, 2019 by the Council of the Institute of Technology, Faculty of Science and Technology, University of Tartu, Estonia.

TABLE OF CONTENTS

LIST OF ORIGINAL PUBLICATIONS

This thesis is based on the following original publications:

I. S. Nakshatharan, U. Johanson, A. Punning and A. Aabloo, "Effect of porosity and tortuosity of electrodes on carbon polymer soft actuators," *Journal of Applied Physics,* 123, 014502, 2018.

II. S. Nakshatharan, U. Johanson, A. Punning and A. Aabloo, "Modeling, Fabrication, and Characterization of Motion Platform Actuated by Carbon Polymer Soft Actuator" *Sensors and Actuators A: Physical,* 283, 87–97, 2018.

III. S. Nakshatharan, V. Vunder, I. Põldsalu, U. Johanson, A. Punning and A. Aabloo, "Modelling and control of ionic electroactive polymer actuators under varying humidity conditions," *Actuators*, 7(1), 7–20, 2018

IV. S. Nakshatharan, J. G. Martinez, A. Punning, A. Aabloo, Edwin W.H. Jager "Soft parallel manipulator fabricated by additive manufacturing"- In Print

Author's contribution

In the publication I, the author developed the electromechanical model, conducted simulation, experimentation, data processing, and analysis. The author was responsible for writing the paper and was the corresponding author.

In publication II, the author simulated, fabricated the manipulator using the spray coating method, characterized and analysed its electromechanical deformation and performed data processing and analysis. The author was responsible for writing the paper and was the corresponding author.

In publication III, the author developed an experimental arrangement, conducted experiments, designed the controller and performed data processing and analysis. The author was responsible for writing the paper and was the corresponding author.

In publication VI, the author printed the manipulators, developed model, conducted experimentation, simulation, and data analysis, and was responsible for writing the paper.

Other papers relevant to this work but not included in the thesis

- A. Epljakov, V. Vunder, E. Petlenkov, S. Nakshatharan, A. Punning, V. Kaparin, J. Belikov, A. Aabloo, "Fractional-order Modeling and Control of Ionic Polymer-Metal Composite Actuator" *Smart Materials and Structures* (Accepted)

- S. Nakshatharan, U. Johanson, A. Punning and A. Aabloo, "Modelling and control of self-sensing ionic electroactive polymer actuator", *Proc. SPIE 10966, Electroactive Polymer Actuators and Devices (EAPAD) XXI, 109661C,* 2019.
- Z. Zondaka, A. Kivilo, S. Nakshatharan, K. A. Küppar, U. Johanson, T. Tamm, R. Kiefer, "Carbide-derived carbon and poly-3,4-ethylenedioxythiphene composite trilayer: linear and bending actuation," *Synthetic Metals*, 245, 67–73, 2018.
- S. Nakshatharan, U. Johanson, A. Punning and A. Aabloo, "Fabrication of Carbon Polymer Composite Manipulated Multi Degree Motion Platform", *Proc. SPIE 10594, Electroactive Polymer Actuators and Devices (EAPAD) XX, 105941Y,* 2018.
- A. Kivilo, Z. Zondaka, S. Nakshatharan, K.A. Küppar, T. Tamm, R. Kiefer "Poly-3,4-ethylenedixoythiophene on carbide-derived carbon trilayer: combined linear actuation characterization" *Proc. SPIE 10594, Electroactive Polymer Actuators and Devices (EAPAD) XX, 105942L,* 2018.
- S. Nakshatharan, A. Punning and A. Aabloo, "A Neural Network Modelling and Sliding Mode Control of Self Sensing IPMC Actuator" *Journal of Intelligent Materials Systems and Structures,* Vol 28, Issue 20, 3163–3174, 2017.
- S. Nakshatharan, U. Johanson, A. Punning and A. Aabloo, "Effect of porosity of the electrodes on ionic electroactive polymer actuators" *Proc. SPIE 10163, Electroactive Polymer Actuators and Devices (EAPAD), 101632I,* 2017.
- S. Nakshatharan, A. Punning and A. Aabloo, "Temperature and humidity dependence of ionic electroactive polymer actuators" *Proc. SPIE 10163, Electroactive Polymer Actuators and Devices (EAPAD), 1016313,* 2017.
- S. Nakshatharan, U. Johanson, A. Punning and A. Aabloo, "Effect of electrical terminals made of copper to the ionic electroactive polymer actuators" *Proc. SPIE 10163, Electroactive Polymer Actuators and Devices (EAPAD), 101632M,* 2017.
- S. Nakshatharan, A. Punning, S. Assi, U. Johanson, A. Aabloo, "Fish-skeleton visualization of bending actuators" *Proc. SPIE 9798, Electroactive Polymer Actuators and Devices (EAPAD), Las Vegas, USA.* 2016, 97981P
- S. Nakshatharan, A. Punning and A. Aabloo, "Neural network modeling and model predictive control of ionic electroactive polymer actuators" *Proc. SPIE 9798, Electroactive Polymer Actuators and Devices (EAPAD), Las Vegas, USA.* 2016, 97982J

ABBREVIATIONS AND SYMBOLS

CDC   Carbide-derived carbon
CNT   Carbon nanotube
CP   Conducting polymer
CPC   Carbon polymer composite
DAP   Direct assembly process
DOF   Degree of freedom
DAQ   Data acquisition
DMSO   Dimethyl sulfoxide
EAP   Electro-active polymer
EDL   Electrical double layer
EDLC   Electric double layer capacitor
EMIM   1-ethyl-3-methylimidazolium (cation)
FEM   Finite element method
IEAP   Ionic electroactive polymer
IL   Ionic liquid
IPMC   Ionic polymer-metal composite
IR   Infrared
LDR   Light dependent resistors
MATLAB   Matrix Laboratory
MIMO   Multi-Input-Multi-Output
MPC   Model predictive control
MWCNT   Multi-walled carbon nanotube
PDE   Partial differential equation
PEDOT:PSS   Poly(3,4-ethylenedioxythiophene) polystyrene sulfonate
PNP   Poisson-Nernst-Planck
PVdF   Poly(vinylidene fluoride)
PVdF(HFP)   Polyvinylidene fluoride-*co*-hexafluoropropylene
SEM   Scanning electron microscopy
SWCNT   Single-walled carbon nanotube
OTf   Trifluoromethanesulfonate (anion)
TFSI   Bis(trifluoromethanesulfonyl)imide (anion)

aC Specific capacitance (F/m^3)
A State matrix
B Input matrix
c_i Concentration (mol/m^3)
$c_\pm$ Concentration of cations and anions (mol/m^3)
C Output matrix
D Feedthrough or feedforward matrix
D_i Diffusion coefficient (m^2/s)
D_{eff} Effective Diffusion Coefficient (m^2/s)
e Electron charge (C)

E	Equivalent bending modulus (Pa)
F	Faraday Constant (C/mol)
h	Thickness of the actuator (mm)
i	Ionic species; either cations or anions (+ or -)
i_0	Exchange current density (A)
i_f	Faradic current (A)
i_1	Electronic current (A)
i_2	Ionic current (A)
i_{dl}	Electric double layer charging/discharging current (A)
J_i	Ion flux
k	Current time
l	Measurement distance from the fixed input contact (mm)
L	Geometrical thickness of the electrode (m)
L'	Diffusion length of ions through the thickness direction (m)
M_s	Molar mass (kg/mol)
N_C	Control horizon
N_H	Prediction time horizon
r	Pore's characteristic dimension (m)
$r(k)$	Prediction of the output displacement (mm)
r_{min}	Minimum actuator displacement output (mm)
r_{max}	Maximum actuator displacement output (mm)
R	Gas constant (J/(K*mol))
R_i	Electrochemical reaction kinetics
T	Temperature (K)
u	Velocity of the flux flow (kg/s^1 m^2)
$u1$	Input vector
$u(k)$	Control signal (V)
u_{min}	Minimum control signal magnitude (V)
u_{max}	Maximum control signal magnitude (V)
V_T	Total volume of the electrode (m^3)
V_{empty}	Volume of empty space (m^3)
W	Tuning Parameter
x	State vector
y	Output vector
$y_m(k)$	Reference signal (mm)
z_i	Charge of species i

Greek alphabet

α_a	Anodic rate transfer coefficients
α_c	Cathodic rate transfer coefficients
β	Bruggeman exponent
β_{ss}	Volumetric swelling coefficient (m^3/kg)
δ	Displacement measured by the displacement sensor (mm)
$\delta 1$	Active particle shape

ε	Strain
ε	Permittivity of the medium (F/m)
ε_o	Permittivity of vacuum (F/m)
ε_{in}	Intercalation strain
τ	Tortuosity
η_e	Charge density (C/m^3)
μ	Dynamic viscosity (Pa*s)
υ	Poisson's ratio
$\in$	Porosity
η	Activation overpotential (V)
ρ	Active particle conductivity (S/m)
ρ_b	Effective ionic conductivity (S/m)
ρ_e	Effective active particle conductivity (S/m)
ρ_p	Density (kg/m^3)
σ	Stress (Pa)
σ_{in}	Intercalation stress (Pa)
σ_M	Mechanical stress (Pa)
σ_T	Total stress (Pa)
Φ_1	Potential at solid phase (V)
Φ_2	Potential at solution phase (V)

1. INTRODUCTION

Ionic electroactive polymers (IEAPs) based actuators are a type of smart composite materials that have the ability to convert electrical energy into mechanical energy or *vice versa* and can be used as sensors and actuators. The actuators fabricated using IEAP materials will benefit from attractive features such as high compliance, lightweight, large strain, low voltage, biocompatibility, high force to weight ratio, and ability to operate in an aqueous environment as well as in the open air [1–3]. The materials can be fabricated in different shapes and can be scaled to operate in microscale. Due to these advantages, the IEAP actuators have been explored for applications in the field of the soft robotic system, especially in the microdomain for cutting edge applications such as micromanipulation systems, medical devices with higher dexterity, soft catheters with built-in actuation, bio-inspired robotics with better-mimicking properties and active compliant mechanisms [1,4–7].

However, there exist significant challenges in understanding their sophisticated electro-chemo-mechanical dynamics, simplifying complex fabrication methods, and developing efficient and reliable control technique to handle their nonlinear behavior. Hence there is a need to develop enhanced modelling methodologies, simple fabrication methods, and robust control scheme to meet the demands of real-time applications in the upcoming field of soft robotics. This dissertation is focused to address these issues by developing an enhanced electromechanical model to understand the charge storage kinetics and to predict the bending displacement of IEAP actuators. Further followed by the use of a simpler additive manufacturing method for high throughput production and developing real-time feedback control for demonstrative micromanipulation applications.

Considering the electromechanical modelling, FEM method is used to describe the ion transport dynamics under electric field by combining the Poisson-Nernst-Planck (PNP) equation and the mechanical response is associated with the volumetric swelling caused by ion intercalation. The model proposed in this thesis gives emphasis to the charge storage mechanism such has double layer charging/discharging and as well as redox process in different types of electrode materials providing the insight view of the underlying electrochemical kinetics in this type of actuators. Also, the framework of the electro-chemo-mechanical model provides the opportunity to predict the behavior of the actuator through 3-dimensional computer simulation. Thereby, this model can be employed to design and simulate complex compliant mechanism using IEAP actuators for soft robotic applications prior to fabrication empowering the opportunity to predict, characterize, visualize and optimize the design parameters. As an example, in this work, a novel parallel soft manipulator with three degrees of freedom was simulated using the model and later fabricated and characterized. It is proved that the developed model was able to predict the behavior of the manipulator with a close agreement ensuring the

high fidelity of the modelling framework. The manipulator is initially fabricated using a spray coating method with a carbon-based electrode and later the same is completely 3D-printed using commercially available conducting polymer and separator material. It is shown that the printing is much simpler to other fabrication techniques and also it allows to design complex and intricate patterns with batch processing ability for high volume production

Finally, as a laboratory scale micromanipulation application, a microscope stage is proposed using the designed manipulator. In order to control the manipulator model predictive control (MPC) system architecture is developed and experimented demonstrating the application. Among several possible controllers MPC control is selected because of their ability to handle embedded constraints such as the safe potential and displacement range, which are important for IEAP actuators and also it can be easily tuned and extended to a multi-input-multi-output system. It is shown experimentally that the developed controller was well capable of predicting and controlling the actuator for micromanipulation application. Overall this work results in enhanced modelling, simple fabrication, and control of ionic electroactive polymer actuators leading to the development of a low cost, monolithic, flat, multi DOF parallel manipulator for micromanipulation application.

2. MOTIVATION AND SCOPE OF THE THESIS

The aim of the research is to develop a physics-based electrochemical model of IEAP actuators addressing some of the fundamental key aspects specific to the type of electrode materials and applying the model to design a soft robotic compliant mechanism. The goal of the research will be achieved by conducting a computational study of IEAP actuators using the FEM method and using the model to design and characterise a soft robotic compliant mechanism and thereof proceeded by fabrication and control for a micromanipulation application. There are two types of electrode materials that are considered for the compliant mechanism namely carbide-derived carbon (CDC) and poly(3,4-ethylenedioxythiophene) polystyrene sulfonate (PEDOT:PSS) with both having PVdF as the separator membrane. Ionic liquids EMIM TFSI and EMIM Otf are used as the electrolyte for CDC and PEDOT:PSS electrodes respectively. Ionic liquids have negligible vapour pressure and therefore do not evaporate and so the actuators can be used in the open air for a long time. Compared to EMIM TFSI, EMIM OTf is hydrophilic in its nature and hence the actuators are highly influenced by environmental humidity conditions.

Below follows a brief description of the studies conducted in this Ph.D. project.

Publication 1: The author has developed an electro-chemo-mechanical model based on the finite element method to describe the IEAP actuators with carbide-derived carbon (CDC) and PVdF separator. Compared to previously published FEM models in the literature, where the electrodes are considered only as flat conductors that provide the electric field, its physical properties and its relation to electronic conductivity, ionic conductivity, and mechanical deformation are not addressed. In this work, the author used porous electrode theory to study the influence of the porous nature of the carbon electrodes on the electrical and mechanical properties of the actuator. Also, in previously published models, based on coupling the Poisson-Nernst-Planck (PNP) equation and linear elastic theory, the basic underlying charge storage mechanism (electrical double layer charging/discharging) is not taken into account with the assumption of no electrochemical reactions taking place in the material. In this work, the electrical double layer capacitive process is addressed using expression relating linear dependence of the charge with changing potential representing the typical electrochemical signature of capacitive electrodes. The electrochemical model is verified using cyclic voltammetry studies and compared with simulation providing deeper insight into the charge storage mechanism. In the mechanical model part, the stress generated in the electrode is attributed to intercalation of ions causing volumetric swelling which is experimentally verified using digital image correlation methodology. Unlike previously proposed models, where the movement of only cations is considered, this model considers both cation and anion movement since the actuator uses a porous PVdF separator membrane,

which is non-ionic in nature. The simple mechanical formulation relates deformation strain to the concentration gradient due to the ionic flux. Thereby the strain is related to the physical properties, such as concentration, diffusion coefficient, viscosity, and mobility of ions, etc. All critical parameters for the simulation, including the Bruggeman's exponent are experimentally measured and the simulation results are compared with experimental results. It is shown that at 60% porosity of electrode the diffusion coefficient of ions reduces to 33.5% compared to that of in bulk ionic liquid. The conductivity of the electrode decreases by a factor of 0.77 compared to bulk conductivity. Also, it is shown that for fixed pore channels and electrode porosity, the ions which are highly active in terms of mobility dominate the resulting deformation direction and rate of deformation in a PVdF membrane. It is the first time the influence of porosity and tortuosity effects on actuation of porous carbon electrode actuators are studied.

The model and the summary of the results are provided in Chapter 4 of the thesis. The same model is used for predicting the electrochemical reaction in the conducting polymer actuators with the inclusion of the Butler-Volmer equation representing faradic reactions. The application of the model to conducting polymer is included in Publication 4 and the summary of results are presented in Chapter 4 of the thesis.

The extension of the model to simulate the complex pattern and the compliant mechanism using IEAP is discussed in Publications 2 and 4 and the summary is provided in Chapters 5 and 6.

Publication 2: The author fabricated, characterized, and modelled a novel ionically driven soft, flat, monolithic parallel manipulator, actuated by CPC actuators. Compared to previous literature regarding manipulation using IEAP actuators where motion is described only in one or two axes, the proposed design in this work can produce three DOF movement that includes linear displacement along one axis and rotational motion along two axes. The manipulator design consists of four CPC actuators supporting a square-shaped central platform at the vertices. The four actuators can be actuated individually or simultaneously in order to move the platform in a desired orientation and position. The manipulator proposed has the main advantage that it is fabricated as a single structure and it does not require any additional support mechanism or linkage to obtain the different degrees of motion. The model proposed in Publication 1 was used for the initial study and structural optimization of the width of the vertices supporting the central platform. The optimization objective is to obtain a maximum strain of the actuators subject to the constraint of minimum twisting/rotation motion with the design variable begin width of the vertices. The maximum displacements and rotation angles over a range of width dimensions are computed and compared for optimum width to provide maximum displacement with a minimum parasitic twisting motion. Later during fabrication, the stage is trimmed to the dimensions obtained through simulation. It is shown experimentally that carbon-based ionic actuators are capable of

generating about ±15 mm linear displacement and ±15° rotational angles along two axes and it is shown that the results closely match the prediction made through simulation. To the author's knowledge, this is the first time, such large displacements and rotational angles in 3 DOF manipulator are achieved within a monolithic structure through geometric design.

The summary of the simulation, fabrication and characterization results are provided in Chapter 5 of the thesis.

Publication 3: The author studied the influence of relative humidity on the electrical and mechanical parameters of the IEAP actuators. The study describes the hydrophilic nature of EMIM-OTf ionic liquid and its influence on electromechanical properties of the actuator. The relative humidity is varied in the range of 10% to 90% in the controlled chamber and the electrical and mechanical properties of the actuator are studied through impedance spectroscopy analysis, cyclic voltammetry and mechanical frequency response and an electrical equivalent circuit using Warburg impedance are represented. There are no such studies conducted on ionic polymer actuators earlier to characterize the actuator under varying degrees of relative humidity conditions to analyze the effect of the hydrophilic property of the ionic liquid. It is shown that from 10% to 90% humidity change, the electrolyte resistance changes from 450 Ω to 20 Ω, the charge transfer resistance changes from 15 Ω to 180 Ω, double layer capacitance changes from 3 μF to 250 μF and peak to peak mechanical displacement changes over 400% respectively on the experimental sample. The study reveals the substantial effects of the ionic liquid's properties on the actuation. Such property of ionic liquid with water results in uncertain actuation of IEAP materials and shows there is a need for encapsulation or control technique to obtain reliable actuation. A possible control technique using a neural network model including humidity has one of the model parameters along with a gain-scheduled MPC control is proposed. Among various control algorithms, MPC is chosen due to its simplicity and ability to handle constraints of the actuation. The developed model and controller are experimentally verified and found to be well capable of predicting and controlling the actuator under humidity conditions varying in the range of 10%–90%.

The control method developed during this study is adapted to control the parallel manipulator design for a micromanipulation application and is described in Chapter 7.2 of the thesis. Also, the study enhanced the need to change the less hydrophilic ionic liquid for the manipulator described in Chapter 6 of the thesis.

Publication 4: The author used the additive manufacturing method including a custom made syringe type printer for fabricating the same manipulator design described in Publication 2 using conducting polymer material. The printing method is selected since the spray coating method discussed earlier is a labour-intensive process and also the actuators fabricated manually do not have uniform characteristics. Also compared to carbon-based actuator fabrication

which requires chemical processing and special carbon materials, this method uses completely commercially available off-the-shelf materials for the fabrication process. It is shown that compared to common techniques, such as direct electrochemical synthesis, spin coating, and drop casting, printing allows to design and fabricate complex and intricate patterns with batch processing ability for high throughout production. Further, it is shown that use of low-cost custom printing based on the syringe-type system provides much freedom in terms of the use of polymer materials compared to printing on inkjet nozzle which requires special ink or requires ink with modified rheological properties with the use of additives. From the modelling perspective of conducting polymer electro-chemo-mechanical dynamics of the printed actuators is described using the model in Publication 1 with the addition of including redox reactions. The model provides a deep insight into the understanding of the capacitance of printed PEDOT:PSS. It is proposed that the underlying electrochemical kinetics is contributed by two different phenomena namely electric double layer charging/discharging and as well as the redox process, whereas it is mostly understood to be only redox process. Though physically it is complicated to measure or separate the charge contributed by each of the processes, through simulation each process is separated and their role on the overall charge transport is studied providing the insight view of the underlying kinetics in this type of actuators. Through simulation and comparing with experimental verification using cyclic voltammetry studies, it is shown the double layer process contributes the most charge and is the dominant phenomenon driving the printed actuators.

Finally, the fabricated manipulator is experimentally characterized and a laboratory scale demonstration of the ability to manipulate the monolithic structure in two different axes is shown through steering light on an X-Y axis and triggering a switch. Though the application shown is not a viable replacement for commercial actuators or optical switch yet, the experiment demonstrates high levels of manipulability along different degrees of freedom from the printed CP actuators which are exceptional within soft ionic actuators fabricated using off the shelf commercially available materials and also keeping the fabrication method simple.

In the final chapter of the thesis, the application of the printed manipulator is extended for a microscope stage application. MPC control developed for Publication 3 is adapted to the microscope stage demonstration of the manipulator and is shown that it can precisely move with up to 100 μm precision. The stage displays better results compared to previously proposed microscope stage using polypyrrole actuators. The very advantage of an ionic polymer based microscope stage is the ability to be operated inside a scanning electron microscope chamber since the actuator can operate in a vacuum and there is no magnetic field to cause parasitic interaction inside the chamber. But the printed actuator at the current stage of research is used under an optical microscope simply as a proof-of-concept demonstration. The actuators need to be down-

sized further and require an integrated sensor for feedback control to be used inside the SEM chamber.

Nevertheless, both applications described in the thesis are laboratory-scale demonstrations to study and explore possible application using ionic actuators. Comparing with the previous attempts to use ionic actuators as a micromirror, autofocus system, microscope stage, etc. that have been proposed in the literature, the geometric configuration provided in this thesis achieves higher displacements and rotation angles. Hence, this soft manipulator is a viable alternative in those applications. Still, for real-world applications, the ionic actuators, bandwidth, reliability, force, fabrication methods, and lifecycles have to be improved.

Overall this research helps in understanding some fundamental electro-chemo-mechanical dynamics related to physical and chemical properties of the electrode materials and their role in the deformation of the actuator. Also, from an application perspective, the model can be used to design, engineer and characterize the behavior of EAP-based soft robotic devices prior to fabrication providing the opportunity to optimize the structural parameters of a device for desired performance.

3. IONIC ELECTROACTIVE POLYMER ACTUATORS

3.1 Overview

Ionic electroactive polymer (IEAP) transducers are a type of electroactive polymer devices belonging to the class of smart materials with applications focusing on soft actuators and sensors [1]. The working principle of IEAPs is mainly based on deformation due to the migration of ions under the applied electric field and the subsequent swelling of the polymer membrane and electrodes. The uneven distribution of ions results in the forces acting at the interface generating a strain difference along the layers of the laminate causing it to deform [8]. This principle has a great potential to develop novel sensors and actuators for the space technology, soft robotics, bio-medical devices, micro/nano manipulation, mechanotransduction of cells, energy harvesting devices, wearable or implantable devices [9]. Moreover, recently there is great interest gained in the research on flexible electronics and all-polymer soft robots to match the great demand for soft, light, biocompatible, quiet, flexible, stretchable and metal-free actuators, and IEAP's perfectly match these requirements [10].

3.2 Classification

Generally, IEAP materials are composed of three key components: electrode, membrane, and electrolyte (or electrolyte solution). Each can be used for classification of IEAPs. According to this principle, the list of the most popular materials for IEAP actuators are grouped by the three components as given in Table 1 [6].

Table 1. Materials for IEAPs.

Membrane	- Ionic polymer, ionomers - Nafion - Flemion - Non-ionic polymers - PVdF - PVdF(HFP) - polyethylene oxide - Polymerized ionic liquids
Electrode	- Metals - Platinum - Gold - Silver - Copper - Carbon - CDC - CNT - Carbon aerogel - Graphene - Metal oxides RuO_2 - ZnO - Conducting polymers - Polypyrrole - Polyaniline - Poly(3,4-ethylenedioxythiophene)
Electrolyte/electrolyte solution	- Water - Water with electrolyte - Metal Cations Na^+ Li^+ K^+ - Organic Cations TMA^+ TBA^+ - ILs - Cations $EMIM^+$ $BMIm^+$ - Anions BF_4^- PF_6^- Otf^- $TFSI^-$ - Polypylene carbonate(PC) with electrolyte - LiTFSI $EMIMBF_4$

3.3 Actuation mechanism in ionic electroactive polymer actuators

The fundamental working principle of IEAP actuators is based on the migration of ions under the applied electric field and the subsequent swelling of the polymer membrane and electrodes. Based on the type of electrode material there arise two different types of driving kinetics, namely electric double layer charging-discharging, and redox reactions. In carbon-based electrode materials, the electric double layer charging and discharging process [11] plays a role in driving the ion transport process. In conducting polymers, the driving kinetics is due to both: electric double layer charging-discharging and redox reactions [12]. In this thesis, the actuators with both types of electrode materials are studied. Their working principles are explained in details below. For the FEM simulation, the ion transport dynamics under electric field is represented by combining the Nernst-Planck and Poisson's equation. The electric double layer charging-discharging is represented by the relation where the charge storage is in a linear relationship with the changing potential within the potential window of interest and Butler-Volmer equation is used to represent the redox process.

3.3.1 Carbon polymer composite

The operation of carbon-polymer composite (CPC) actuators is mainly based on the principle of electric double-layer charging and discharging phenomenon. It is considered that there are no faradaic processes taking place. In case of the electric double layer capacitance, there is no electron transfer across the electrode/electrolyte interface and the charge storage is purely electrostatic. Charge accumulation is achieved electrostatically by positive and negative charges on interfaces which are separated by an ion permeable membrane [13]. This non-faradic charge storage relies on an ideal capacitive behavior of the electric double-layer. Hence, the actuator concept is similar to that of the electric double-layer capacitors [11]. This charge accumulation at the interface of the electrode and electrolyte generates a volumetric swelling resulting in the deformation of the actuators. The schematic representation of the CPC actuator is shown in Figure 1.
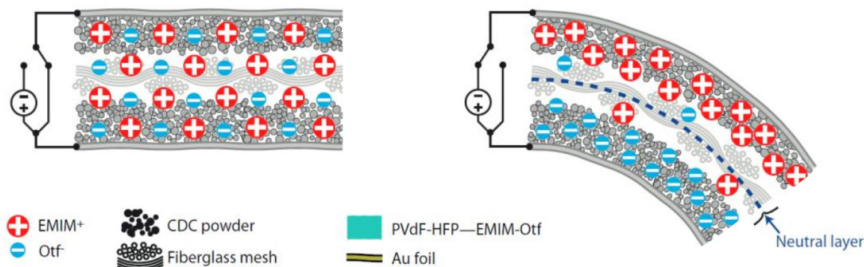

Figure 1. Graphical representation CPC actuation

3.3.2 PEDOT:PSS conducting polymer

In conducting polymer (CP) actuators electron transfer takes place across the electric double layer and the charge storage is achieved by chemical oxidation and reduction states [12]. Upon applying potential, there is an electrochemical change causing oxidation of the polymer chain resulting in the extraction of cations from polymer matrix into the electrolyte to maintain charge balance. This process is reversed on the opposite electrode reducing the conducting polymer to its neutral state resulting in the insertion of cations into the matrix. The ingress and egress of ions and their solvate shells between the polymer matrix and the associated electrolyte to balance the charge cause swelling or contraction of the polymer, which leads to volume change and subsequent bending [2,3,14]. The schematic representation of CP actuator is shown in Figure 2.
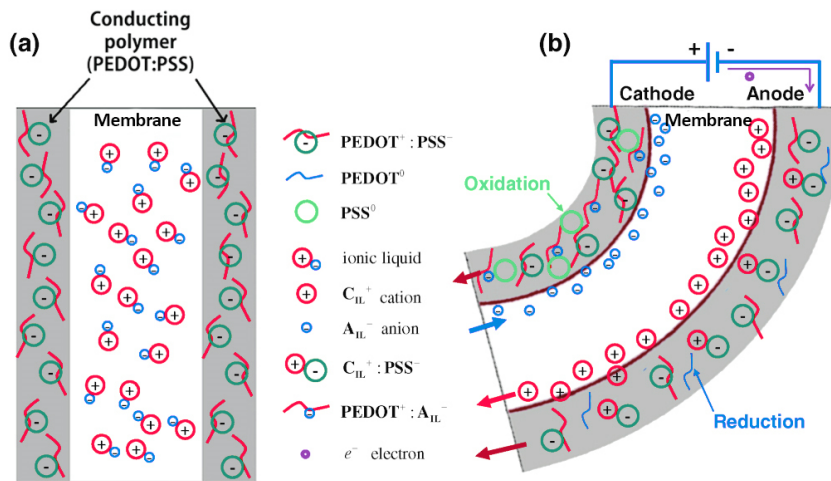

Figure 2. Graphical representation CP actuation[1] (a) Actuator in steady state (b) Under applied voltage [15]

---

4. ELECTROMECHANICAL MODELLING

Considering modelling of the electroactive polymer actuators there are different methodologies based on different aspects of the working principle. They include:

- Bending beam method [16,17] related to the mechanical study of solid state beam bending;
- Equivalent circuit model [18,19] where the electrical equivalent circuit is developed giving a similar electrical response of the actuator;
- Electrochemical model based on faradic conditions that use a linear relationship between applied current and angular movement [20,21];
- Finite element modelling method (FEM) [7,8,22–29].

In this dissertation, electro-chemo-mechanical model using the finite element method was used to describe the charge transport electrochemical response coupled to the mechanical response caused by volumetric swelling. The model can be divided into two distinct parts:

a) The electrochemical response *i.e.* ion transport process upon the application of electrical potential;
b) Resultant mechanical deformation of the actuator.

4.1 Ion transport process

The underlying phenomenon of actuator behavior is based on the ion transport process. Under the electric field, this transport process is described using the Nernst-Planck equation [30] as given below

$$\vec{J_i} = -D_i \vec{\nabla} c_i - \frac{z_i F}{RT} D_i c_i \vec{\nabla} \Phi_2 + c_i \vec{u}, \ (i = +, -) . \tag{1}$$

The equation relates ion molar flux for ionic species i to its concentration, electric potential, and the fluid velocity at any point within the domain. Here J_i, D_i, c_i, Φ_2, and u represent ion flux, diffusion coefficient, concentration of ions, potential at electrolyte and velocity of flux respectively. The subscript i corresponds to ionic species – either cations or anions. The constants z, F, R and T represent charge, Faraday constant, gas constant and temperature respectively. The initial concentration of ions is measured by measuring the weight of the ionic liquid in the sample followed by calculating number of a moles on the sample. In applying the Nernst-Planck equation to an ionic solution or liquid, the electric potential Φ_2 will be determined by the charge density within the domain. Mathematically, this can be expressed using the Poisson's Equation

$$\nabla^2 \Phi_2 = -\frac{\eta_e}{\varepsilon \varepsilon_o} , \tag{2}$$

where ε and ε_o are permittivity of the medium and vacuum respectively, and η_e, the charge density is given by

$$\eta_e = e(c_+ - c_-) \,. \tag{3}$$

In order to evaluate the fluid velocity component u, Navier-Stokes equation with the assumption that flux flow is laminar is used. The velocity of the flux is given by

$$\rho_p \, \frac{\partial u}{\partial t} + \rho_p \, u . \nabla u = -\nabla p + \nabla . \left(\mu (\nabla u + (\nabla u)^T) + F_l \,. \tag{4}$$

A portion of the fluid is pulled along as the ions within that portion are subject to the electric forces. The force acting upon the fluid is given by

$$F_l = (c_+ - c_-)F(\nabla \Phi_2) \,. \tag{5}$$

4.2 Influence of porosity of the electrodes

The finite element models of ionic electroactive polymer actuators proposed earlier in the literature [24,25,27,28,30,31] do not consider the physical and electrical properties of the electrodes and their relation to actuation. The models assume electrodes are only flat conductors that provide the electric field. However, Porfiri showed that the electrode morphology does significantly affect the charge dynamics and hence the actuation performance of the actuator [32]. Though some studies address the problem [29,33,34] a standardized result on the influence of electrode morphology is not yet available. This is, however, essential for carbon-based actuators where the electrode is highly porous compared to a typical IPMC. The effect of tortuosity and porosity on the physical and electrical properties of the electrode and separator have not been observed in the prospect of actuator applications. Hence the influence of the porous nature of the electrodes on the performance of the actuator is addressed using the porous electrode theory.

The two main factors that determine the effective ion transport through the porous electrode are tortuosity and porosity [35]. Mathematically, tortuosity is given by
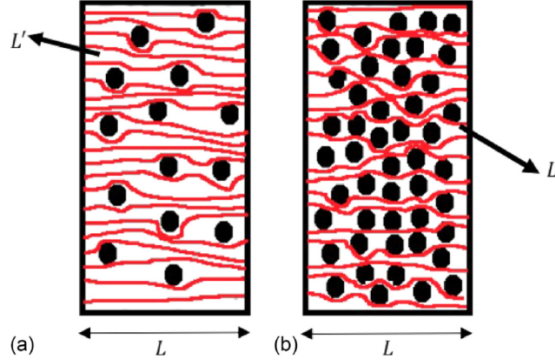
$$\tau = \frac{L'}{L} \,. \tag{6}$$

Figure 3. Porosity of electrodes with ion movement representation (black dots represent electrode particles and the red lines present the ion transport path) (a) Low porosity (b) high porosity

It is the arc-chord ratio of the diffusion length of ions L' to the thickness of electrode L. The factors determining tortuosity are particle size, ion size, membrane pore size, dispersity of particles, shape anisotropy, the thickness of the electrode, *etc.*

The porosity is defined as the ratio of the volume of empty space V_{empty} to that of the total volume of the electrode V_T and is given by

$$\epsilon = \frac{V_{empty}}{V_T}. \tag{7}$$

The Bruggeman relation [35] gives the relation between porosity and tortuosity as

$$\tau = \epsilon^{-\beta} . \tag{8}$$

Here β is the Bruggeman exponent.

The effective conductivity of the porous electrode includes both conductivity of active particles and the spaces occupied by ionic liquid resulting in forming a matrix of active material and electrolyte [36,37]. The effective electrode conductivity accounting for the effect of porosity and tortuosity can be approximated as

$$\rho_e = \frac{(1-\epsilon)\rho}{\tau} . \tag{9}$$

The electronic current conduction in the solid electrode phase by using Ohm's law is

$$i_1 = -\rho_e \nabla \Phi_1 . \tag{10}$$

The ionic current due to the charge carried by ionic species is obtained by summing the currents of both ionic species:

$$i_2 = F \sum_i z_i J_i . \tag{11}$$

Substituting ion flux of each species, Eq. 1 into Eq. 11 and considering the effect of tortuosity and porosity yields that the ionic current is

$$i_2 = -\rho_b \nabla \Phi_2 - z_i F \left(D_{eff+} - D_{eff-} \right) \in \nabla c_i + \left(\sum_i c_i F \vec{u} \right) . \tag{12}$$

Here, D_{eff+}, D_{eff-} are the new effective diffusivities of cations and anions due to the porosity effect in the porous medium and are given by

$$D_{eff\,i} = D_i \frac{\in}{\tau} \ (i = +,-) \ . \tag{13}$$

The new effective conductivity of the electrolyte in the bulk medium is given by

$$\rho_b = F^2 \sum_i \frac{z_i^2 D_{eff\,i} c_i}{RT} \ . \tag{14}$$

Eq. 9 and 14 provide the change in the electrode and ionic conductivities due to the influence of porosity and tortuosity effects respectively and Eq. 13 addresses the change in the diffusion coefficient of ions due to the porous carbon electrode structure.

4.3 Electrochemical kinetics

As described earlier, based on the type of electrode materials there arise two different types of the electrochemical kinetics, namely electric double layer charging and faradic reactions. Considering the previously proposed FEM models [8,25,28,30,38,39] for electromechanical transduction relating PNP equation and mechanical deformation neglect the electrochemical reactions or kinetics. But the electrochemical charge storage mechanism is essential to understanding the actuation mechanism. Therefore, here both the electric double layer charging/discharging and redox processes are addressed to provide a deeper insight into the understanding of charge storage mechanisms.

4.3.1 Electric double layer capacitance

For the CPC actuator at the interface between the matrix and the solution, the rate of change of the electric double layer charge [40] is given by relation stating the linear dependence of the charge with changing potential representing the typical electrochemical signature of a capacitive electrode [41].

$$i_{dl} = aC \frac{\partial(\Phi_1 - \Phi_2)}{\partial t} \ , \tag{15}$$

where aC is the specific capacitance, Φ_1 and Φ_2 are potentials at the solid and solution phases respectively.

4.3.2 Redox process

For conducting polymer electrode the electrochemical kinetics can be considered as a two-phase system with both electric double layer charging/discharging as well as redox reactions. This characteristic feature of the hybrid mechanism is used to develop conducting polymer-based supercapacitors or electric double layer capacitors [13,42–44]. But there have previously been no attempts to include the hybrid mechanism in the modelling of conducting polymer-based actuators. The model addressed in this thesis includes both the types of charge storage mechanism. The faradaic current due to redox reactions can be represented using the Butler-Volmer electrochemical kinetic expression [44]. The electric double layer charging effect is described by the relation as represented in Eq. 15. The faradic current i_f is given by,

$$i_f = i_0 (e^{\frac{\alpha_a F \eta}{RT}} - e^{\frac{-\alpha_c F \eta}{RT}}), \tag{16}$$

where i_0 is exchange current density which is due to the faradic activity even under equilibrium where the net current is zero [45], α_a and α_c are the anodic and cathodic rate transfer coefficients which is the measure of the symmetry of the energy barrier [45], and η is activation overpotential (V) which is the potential difference above the equilibrium potential required to overcome the activation energy to produce specified current [46]. The values of anodic and cathodic rate transfer coefficients are equal(α_a, $\alpha_c = 0.5$) in conducting polymer as it exhibits symmetry [20].

4.4 Charge and material balance conditions

The overall charge balance under the assumption of electroneutrality [47] is given by Eq. 17, stating that the divergence of the total current density in the system is zero.

$$\nabla \cdot i_1 + \nabla \cdot i_2 = 0 \ . \tag{17}$$

For CPC actuators, at the interface between the electrode matrix and the solution, the rate of change of electric double layer charge [47,48] is given by

$$\nabla i_2 = (aC \frac{\partial(\Phi_1 - \Phi_2)}{\partial t}) \; . \tag{18}$$

And for CP actuators, the rate of charge in the system is due to both the process of electric double layer charge and redox reactions [47] and is given by

$$\nabla i_2 = (aC \frac{\partial(\Phi_1 - \Phi_2)}{\partial t} + i_0 \left(e^{\frac{\alpha_a F \eta}{RT}} - e^{\frac{-\alpha_c F \eta}{RT}} \right)) \; . \tag{19}$$

Finally, the material balance equation by conservation of mass [40] is given by

$$\frac{\partial c_i}{\partial t} + \nabla j_i = R_i \; , \tag{20}$$

where R_i is the source term that represents the electrochemical reaction kinetics. It is expressed as

$$R_i \; = \frac{aC}{z_i F} \frac{\partial(\Phi_1 - \Phi_2)}{\partial t} \;\; \text{for CPC.} \tag{21}$$

$$R_i \; = \frac{aC}{z_i F} \frac{\partial(\Phi_1 - \Phi_2)}{\partial t} + \frac{i_0}{z_i F} \left(e^{\frac{\alpha_a F \eta}{RT}} - e^{\frac{-\alpha_c F \eta}{RT}} \right) \; \text{for CP.} \tag{22}$$

4.5 Mechanical response

Generated stress and the resulting strain in the electrode is one of the highly studied areas in many fields including lithium-ion batteries and supercapacitors. In the case of IEAP actuators obtaining large strain and stress is one of the desired factors. Gawith *et al.* studied electrochemical stiffness in lithium-ion batteries and concluded stress scales with intercalation rate and strain scales with capacity [49]. In the previously published models of IEAP relating PNP equation to linear elastic theory [29,30,38] coupling between the electro-chemical processes and mechanical deformation is realized using an experi-mentally determined coupling coefficient that relates the charge and displacement. In this work, the deformation is predicted through the intercalation stress caused by ion transportation and resulting volumetric swelling of the electrode. The volumetric swelling and shrinkage of the electrodes were experimentally verified by Punning *et al.* using the digital image correlation methodology [17] conducted on IEAP actuators. Based on the experimental verification, the mechanical model proposed in this thesis assumes that the stress generation is due to intercalation of ions causing volumetric swelling of the electrodes that results in bending strain.

The constitutive relation, Hooke's law was used to relate stress and strain in the actuator:

$$\sigma = E\varepsilon \, . \tag{23}$$

The overall total stress generated in the material is given by

$$\sigma_T = \sigma_M - \sigma_{in} \, . \tag{24}$$

This relation indicates that the mechanical stress acts in the direction opposite to that of intercalation stress. The intercalation stress is directly related to the strain caused by the swelling of the electrode

$$\sigma_{in} \, \alpha \, \varepsilon_{in} \, . \tag{25}$$

The ε_{in} is the strain generation due to ion intercalation and resulting mass imbalance as given in Eq. 26. Mass imbalance is caused by the concentration difference of total migrating cations and anions:

$$\varepsilon_{in} \, \alpha \, (c_+ - c_-) \, , \tag{26}$$

$$\varepsilon_{in} = \beta_{ss} \, M_s(c_+ - c_-) \, , \text{or} \; \varepsilon_{in} = \beta_{ss} \, M_s \Delta c_{diff} \, , \tag{27}$$

where β_{ss} is the swelling coefficient relating the strain and ion concentration. This model can be used to predict the deformation direction based on the properties of cations and anions, since the actuators can be both cation-driven and anion-driven in a non-ionic membrane like PVdF. Based on the properties, such as the diffusion coefficient, size of ions and pore channels, the respective movement of ions and thereby deformation direction is established. Bending in the opposite direction after initial bending called as back relaxation is typical for this kind of materials. This can be related to the slow-moving counter ions. From Eq. 27 ions with higher diffusion coefficient will migrate faster and the counter ions which move slower cause the back relaxation process [6,50].

The stress-strain relation for the material in 3D geometry is given below

$$\begin{bmatrix} \sigma_{xx} \\ \sigma_{yy} \\ \sigma_{xy} \end{bmatrix} = \frac{E}{(1+v)(1-2v)} \begin{bmatrix} (1-v) & v & 0 \\ v & (1-v) & 0 \\ 0 & 0 & (1-2v) \end{bmatrix} \begin{bmatrix} \frac{\partial u}{\partial x} \\ \frac{\partial v}{\partial y} \\ \frac{1}{2}\left(\frac{\partial u}{\partial y} + \frac{\partial v}{\partial x}\right) \end{bmatrix} - $$
$$\frac{E\beta \Delta c_{diff}}{1-2v} \begin{bmatrix} 1 \\ 1 \\ 1 \end{bmatrix} \, . \tag{28}$$

The time-dependent deformation is given by the PDE

$$\rho_p \frac{\partial^2 u}{\partial t^2} - \nabla . \sigma = F \ . \qquad\qquad (29)$$

4.6 Experimental verification

The finite element simulations with COMSOL Multiphysics were carried out for the actuators and compared with experimental results to verify the developed model.

4.6.1 Electrochemical Simulation

In order to verify the electrochemical kinetics in the proposed model and to understand the charge storage mechanism, electrochemical experiment and simulation were performed through cyclic voltammetry studies.

4.6.1.1 CPC actuator

Experiment and simulation are carried out for an actuator with dimensions: length 4 cm; width 1 cm; thickness 278 μm. Both electrodes are 118 μm thick and the thickness of the separator is 42 μm. The model parameters used for the simulation are listed in Table 2 (Appendix). The following assumptions are considered during the modelling of the actuators.
1. Temperature effects are negligible
2. The porosity of the electrode is constant
3. No electrochemical side reactions occur in the system
4. All mechanical parameters remain constant
5. No change in the electrode and ionic conductivities during actuation

Cyclic voltammetry measurements were conducted on the CPC actuator with EMIM-OTf ionic liquid at a scan rate of 50 mV/s with two different potential windows of ±1 V and ±2 V and the same were simulated using COMSOL cyclic voltammetry simulation studies. Figure 4(a) shows the applied potential at 50 mV/s with a potential range from -2 to 2 V and Figure 4(b) shows the charging and discharging current contributed by the double layer charging and discharging processes. Figure 4(c) compares the CV results from the simulation with experimental results. Comparing the experimental and simulation, the results closely match each other endorsing the double layer charging and discharging as the main phenomenon in CPC actuators. The charge density calculated through experimentation and simulation is 836.04 mC/cm^2 and 825.43 mC/cm^2.
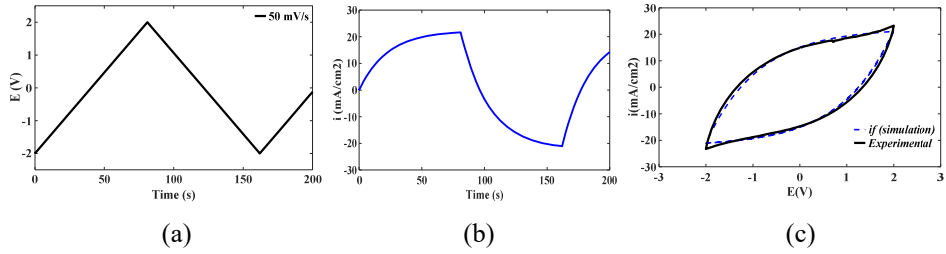
(a)   (b)   (c)

Figure. 4. (a) ±2 V applied potential at 50 mV/s (b) Simulation of current density representing double layer current with respect to time (c) Cyclic voltammetry simulation compared with experimental results.
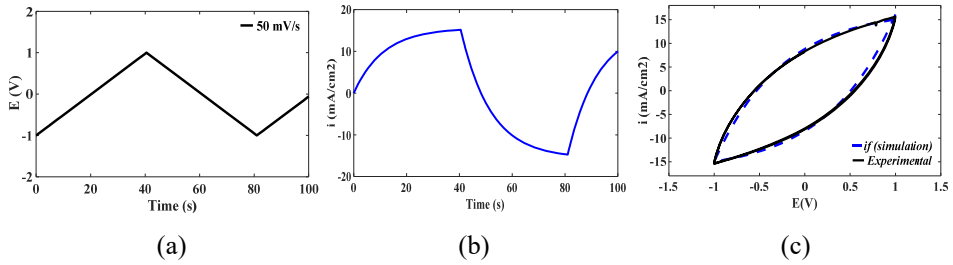

(a)   (b)   (c)

Figure. 5. (a) ±1 V applied potential at 50 mV/s (b) Simulation of current density representing double layer current with respect to time (c) Cyclic voltammetry simulation compared with experimental results.

Under the potential window of ±1 V, the total charge calculated from experimental results is 239.21 mC/cm^2 and that from the simulation is 233.44 mC/cm^2 respectively. In both cases, the experimental results show a higher charge density and are attributed to some parasitic faradic reactions which are not considered in the model.

4.6.1.2 CP actuator

The experiment and simulation were conducted on the CP actuator and the results are shown in Figures 8–11. The actuator under test had the following dimensions: length 2 cm; width 0.5 cm; thickness 155 μm. Both electrodes were 15 μm thick and the thickness of the separator was 125 μm. The model parameters used for the simulation are listed in Table 3(Appendix). The following assumptions are made while modelling the actuator

1. Temperature effects are negligible
2. The electrodes are considered as uniformly flat solid conductors since the thickness of the electrodes is very small compared to that of the separator and it is assumed that all reactions take place at the boundary between the electrode and the separator.
3. No electrochemical side reactions occur in the system
4. All mechanical parameters remain constant

5. No change in the electrode and ionic conductivities occur during actuation

In the case of CP actuators, it is difficult to separate electric double layer and redox processes experimentally to determine the charge contributed by each of the processes. But through simulation using the proposed model, these processes can be separated providing insight into the underlying mechanisms and also helps to understand the individual charge contribution made by the completely different kinetics.

To study the involvement of both double layer charging/discharging and redox process, first the simulation is performed with both processes taking place simultaneously (Eq. 15 and Eq.16 are used in simulation) and subsequent simulation was performed with each process individually (either Eq. 15 or Eq.16 are used) while the other was being suppressed. Figure 6(a) shows the applied potential at 50 mV/s in the potential range from -2 to 2 V and Figure 6(b) shows the current contributed by each of the processes individually as well as the total current contributed by both processes. Figure 6(c) shows the CV results of simulations of each process compared with the experimental results. It is seen summing up the current contributed by both the process the simulation matches closely with the experimental results.

From Figure 6(c), the total charge density calculated through simulation is 124.29 mC/cm^2, the double layer charge and faradic contributions calculated individually are 105.92 mC/cm^2 and 18.372 mC/cm^2 respectively. While experimentally calculated charge density is found to be 111.4 mC/cm^2. Under the potential window of ±1 V, the total charge calculated from experimental results is 44.562 mC/cm^2 and the simulated values are 48.90 mC/cm^2, out of which the faradic process and double layer process charge contribution are 2.68 mC/cm^2 and 46.22 mC/cm^2 respectively.

It is found that the double layer capacitance contributes more charge compared to the redox process in both the potential range of ±2 V and ±1 V. From the results, it is seen that although there exists the involvement of both the processes, the charge contributed by the double layer mechanism is the most dominated effect in the printed actuators.
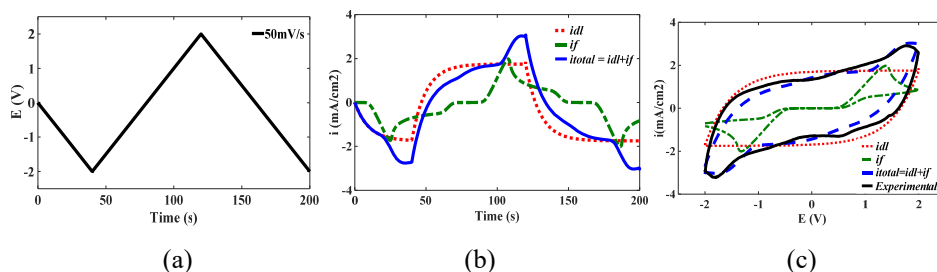

   (a)   (b)   (c)

Figure. 6. (a) ±2 V applied potential at 50 mV/s (b) Simulation of current density representing double layer current, faradic current and total current with respect to time (c) Cyclic voltammetry results compared with experimental results.
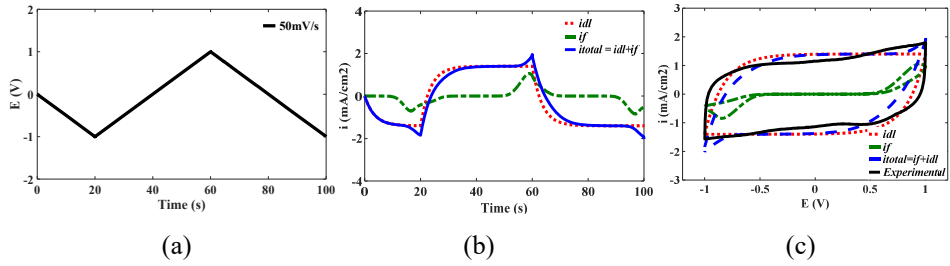
Figure. 7. (a) ±1 V applied potential at 50 mV/s (b) Simulation of current density representing the double layer current, faradic current and total current with respect to time (c) Cyclic voltammetry results compared with experimental results.

4.6.2 Electro-Mechanical Simulation

The experimental setup for verifying the electromechanical simulation is shown in Figure 8. A National Instruments PCI 6036 DAQ device interfaced with PC running MATLAB is used to collect the measurement data. The experiment is conducted at three different step voltages: 0.5 V, 1.0 V, and 2 V. The measured parameters were the current and mechanical displacement while the strain is calculated from displacement [17] using the following equation.

$$\varepsilon = \frac{2\delta h}{l^2 + \delta^2}, \tag{30}$$

where h is the thickness of the actuator, δ is the displacement measured by the displacement sensor and l is the measurement distance from the fixed input contact.
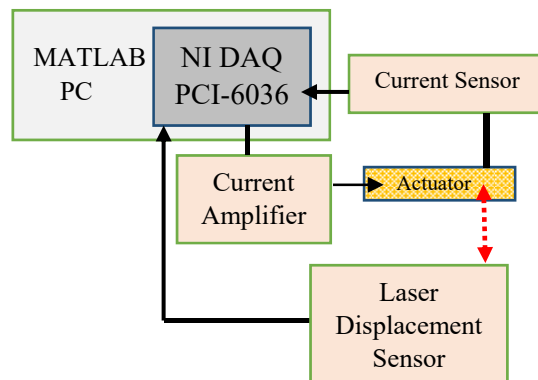

Figure. 8. Experimental setup

4.6.2.1 CPC actuator

For typical electromechanical studies, square wave potential is applied to study the dynamics of the actuator. The applied input signal is shown in Figure 9(a–c) and the corresponding resulting current both from experimental and simulation is shown in Figure 10(a–c). Under applied potential, the ion transport process causes the spatiotemporal distribution of charge density, this distribution of charge density within the material gives rise to charges that collect at the faces of the electrodes. The charges that accumulate at the surface induce an electric current that can be measured across the thickness of the material and is denoted as isothermal transient ionic current [30]. The strain due to the volumetric swelling is shown in Figure 11(a–c).
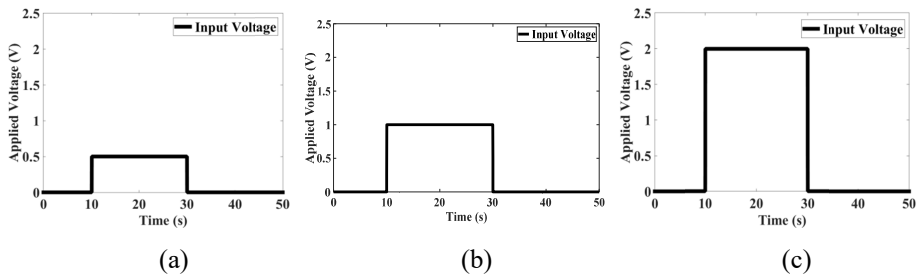
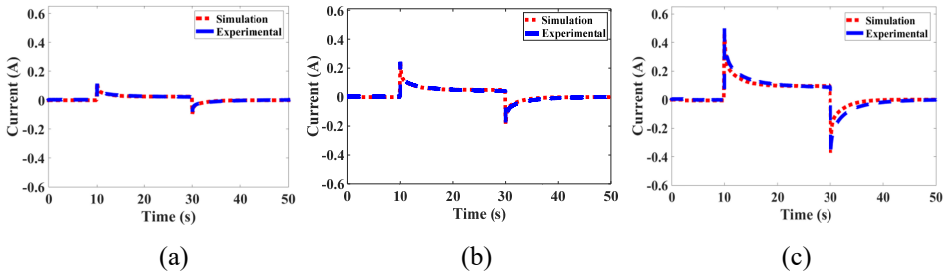**Figure 9**. Applied potential (a) 0.5V (b) 1V (c) 2V

Figure 10. Current profile (a) at 0.5V (b) at 1 V (c) at 2V
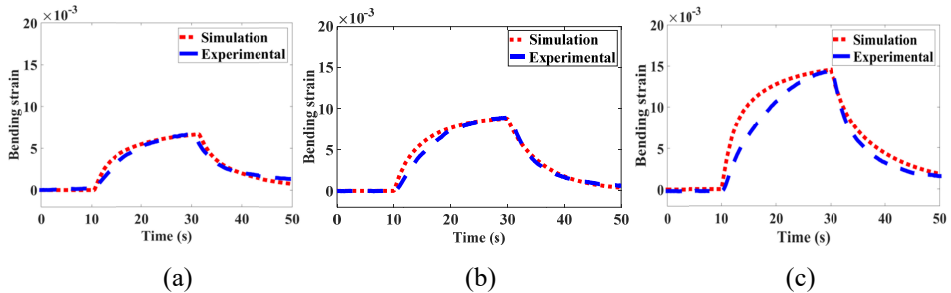
Figure 11. Bending Strain (a) at 0.5 V (b) at 1 V (c) at 2 V

4.6.2.2 CP actuator

Similar electromechanical studies are also performed on CP actuators. Apart from the electrochemical kinetics, the mechanical model is similar to that of the carbon-based actuators. The volumetric swelling parameter is determined from experimentation of the CP actuators and is found to be $1.3*e^{-5}$ m^3/Kg.
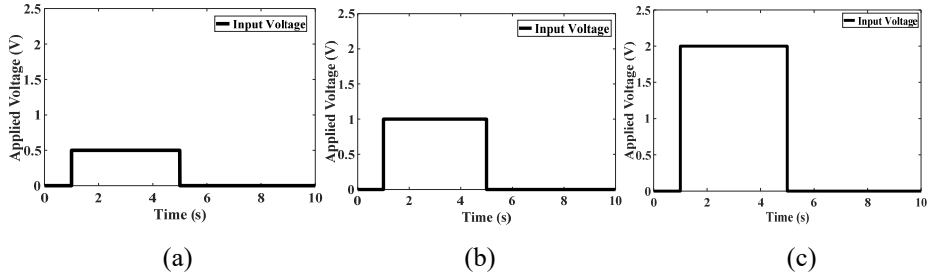

Figure 12. Applied potential (a) 0.5 V (b) 1 V (c) 2 V
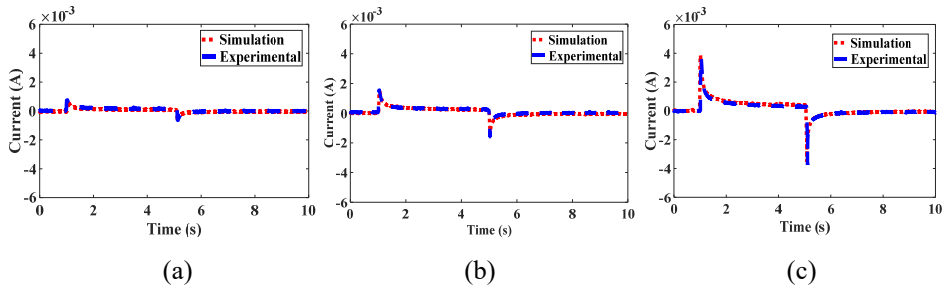
Figure 13. Current profile (a) at 0.5 V (b) at 1 V (c) at 2 V
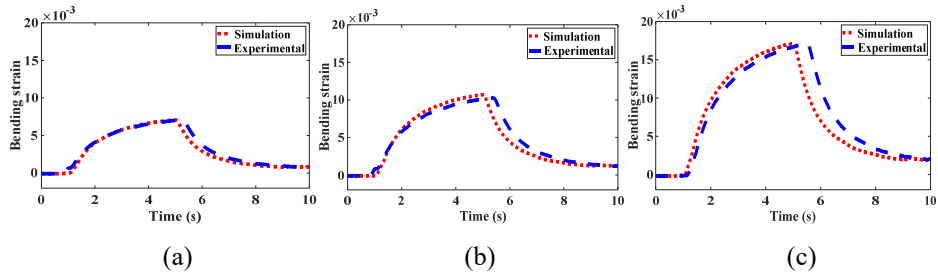
Figure 14. Bending Strain (a) at 0.5 V (b) at 1 V (c) at 2 V

In both the CP and CPC simulation, a good agreement is achieved between predicted displacement and experimental results at lower voltages such as 0.5 V and 1 V, but at 2 V the discrepancies increase, and it is assumed it is due to the additional faradic reactions such as electrolysis of water absorbed from surroundings, which is not considered in the model. Hence the major limitation

of the proposed model is that it can be used to predict small displacements and voltages up to 2 V. Beyond 2 V the displacement is highly non-linear and the model fails to capture the dynamics of the actuator. Another limitation of the model is that the influence of humidity on the properties of actuation is not addressed. Hence at very high or low humidities, the change in the viscosity of the ionic liquid and the diffusion coefficient of ions is not included in the model and hence the model will fail to predict the actuation under varying humidity conditions.

5. SOFT PARALLEL MANIPULATOR MODELLING AND FABRICATION

5.1 CPC soft parallel manipulator

In chapter 4, the FEM-based electromechanical modelling of ionic electroactive polymer actuators is described. The model can be applied and used in different approaches as follows: a) to describe the sophisticated background of the electro-chemo-mechanical dynamics enhancing a deeper understanding of the working principle, b) simulate and measure the governing parameters that are not possible to physically measure otherwise, c) design, engineer and characterize the behavior of EAP-based soft robotic devices prior to fabrication providing the opportunity to optimize structural parameters such as thickness, length and width of the actuator for obtaining desired performance. In this chapter, a novel soft parallel manipulator application based on EAP actuators is modelled, fabricated and characterized. The developed finite element model is used to determine the thickness of the connecting joints on the manipulator and to characterize its workspace before the fabrication process. This methodology helps in removing the traditional trial and error approach avoiding wastage of materials and also reduces the fabrication time required for obtaining a device with optimal dimensions.

Most of the IEAP applications are limited to bending actuation. However, the bending motion can be translated to multiple degrees of motion by using the appropriate design of multiple actuators connected together or by using external support mechanisms such as gears and pulleys. But the use of an external support mechanism with the soft actuators increases the complexity of the system. Also fabricating very small lightweight components and joint connections is quite complicated. Hence, configuring the actuators themselves for obtaining the different degrees of motion in a monolithic structure is highly preferred. Such soft monolithic body is the aim of the emerging field of biologically inspired robotics or soft robotics systems [7].

A novel monolithic configuration of the ionic actuator for a soft robotic manipulator application with multiple degrees of freedom is proposed in this chapter. It consists of four actuators supporting the square shaped central reinforcement grid at the vertices as shown in Figure 15(a). The four actuators can be actuated individually or simultaneously in order to move the platform to a desired orientation and position. The different degrees of motion produced by the mechanism is shown in Figure 15(b).

The proposed design is over-actuated *i.e.* four actuators are used for three degrees of freedom. Geometrically three actuators are optimum for obtaining three degrees of motion forming a triangular structure. But the main constraint in fabricating the three actuator manipulator arises from the plain woven pattern of the glass fiber used as the supporting structure. The glass fiber weave pattern needs to be aligned with the actuator bending direction for uniform bending

along the length. But in case of a three actuator design, the weave pattern will be random for each actuator and hence each actuator will behave differently. Hence, due to practical consideration, a four-actuator design is considered.
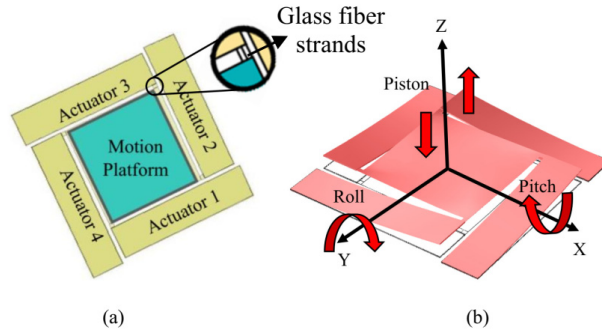

Figure 15. Graphical representation of the actuator: (a) proposed configuration; (b) degrees of freedom.

5.2 Modelling of the manipulator

The connection point between the vertex of the central reinforcement grid and the actuator is held by glass fiber strands that act as spherical joints providing the platform with the necessary degrees of freedom as shown in Figure 15(b). The proposed structure is modelled using COMSOL Multiphysics. The thickness of the vertices is varied over a range with the consideration of maximum strain and minimum twisting and simulated for each possible dimension. It is found that more than three glass fiber strands connecting the platform and the actuator will restrict the motion of the system and thereby the displacement of the platform obtained would be considerably lower. On the other hand, only one glass fiber between the actuator and platform leads to larger displacements but introduces additional twisted motion resulting in non-uniform displacements along the platform surface. With three glass fiber strands between the platform and actuator, the additional non-uniform motion is eliminated while the sufficiently large displacements are achieved.

From the model, the actuation of the device in three degrees of motion is predicted for its maximum displacement and bending angles. The results of the simulation are shown in Figures 16(a), 16(b) and 16(c), depicting linear, roll and pitch motion respectively. From Figure 16(a) the linear displacement obtained using simulation is ±16 mm and the maximum rotation angles achieved along both axes are ±18 degrees and are shown in Figure 16(b) and 16(c). With satisfactory large displacements and rotation angles predicted from the model, the fabrication of the device proceeds.
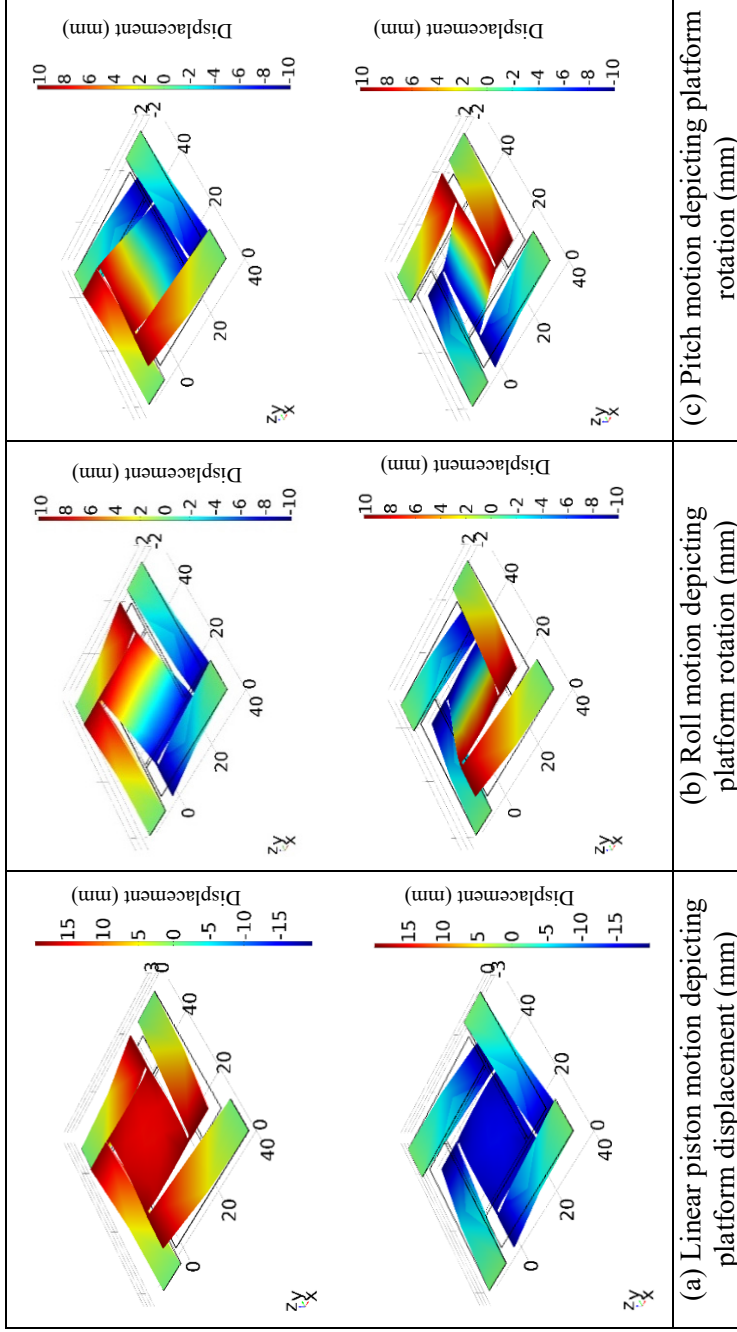
Figure 16. FEM simulation of the mechanism

(a) Linear piston motion depicting platform displacement (mm)

(b) Roll motion depicting platform rotation (mm)

(c) Pitch motion depicting platform rotation (mm)

5.3 Fabrication of the proposed configuration

The actuator is fabricated based on the methods and materials described in detail by Kaasik *et al.* [51]. In this section, more specifically the method of fabrication of the manipulator alone is described.
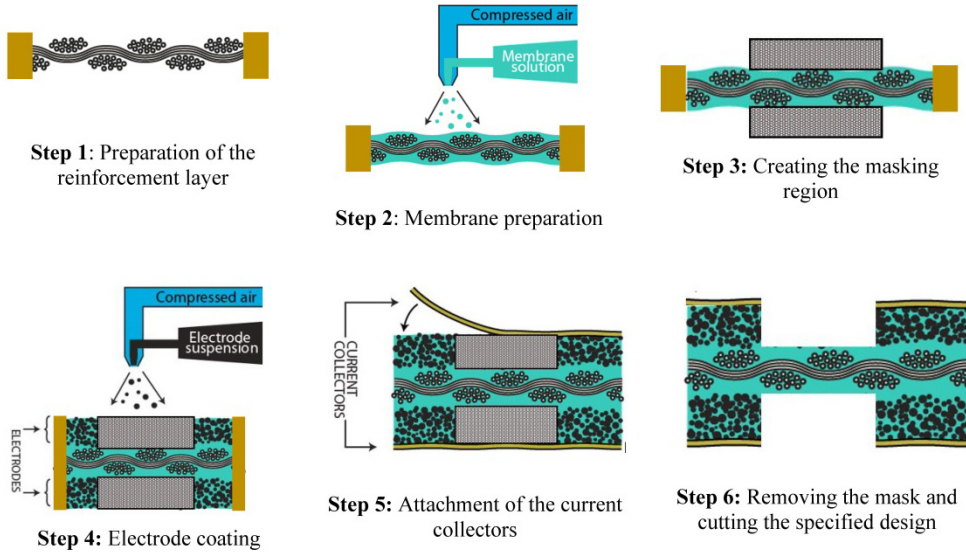

Figure 17. Steps of the fabrication process

First, a thin inelastic glass fiber reinforcement grid (18 g/m^2) was tautened to a circular frame. This layer maintains in the neutral position and aids in obtaining a controlled and predictable actuation in both directions. A mixture of EMIM-Otf (50 wt%) and PVdF-HFP (50 wt%), dissolved in 4-methyl-2-pentanone was applied on the tautened reinforcement grid using the spray coating technique and the solvents were evaporated using a hot air gun. The spraying procedure was repeated until the membrane of the desired thickness was achieved. The platform region is masked with 100 μm thick plastic film of size 25 x 25 mm^2 held by small neodymium magnets on both sides of the membrane. The electrode suspension, containing fine powder of CDC (30 wt%), EMIM-OTf (35 wt%) and PVdF-HFP (35 wt%) dissolved in N,N-dimethylacetamide, was deposited on both sides of the masked grid-reinforced membrane using the spray coating method. The process was repeated until the electrode of the desired thickness was achieved. The thickness of each electrode was 140 μm and the separator was 50 μm.

After the structure was released from the support, the current collectors were glued to the surface as described in previous studies [10,51,52]. The last step was removing the mask and slitting the structure to the desired shape. The actuator is split from the central stage leaving three strands of glass fiber

membrane to connect the actuator and each vertex of the platform. Each actuator is 40 mm long and 10 mm wide and supported by specially designed clamps to provide an electrical connection. An additional glass slide is placed on the surface of the platform since the thin membrane and glass fiber alone are unstable and will cripple during actuation. But the addition of a glass slide act as a payload and limits the maximum achievable movements.

Figure 17 describes the schematic representation of the fabrication steps, Figure 18(a) shows the picture of the platform with mask, Figure 18(b) shows the platform removed from frame, Figure 18(c) shows the actuator after applying gold current collectors and Figure 18(d) shows the final platform attached to the frame.
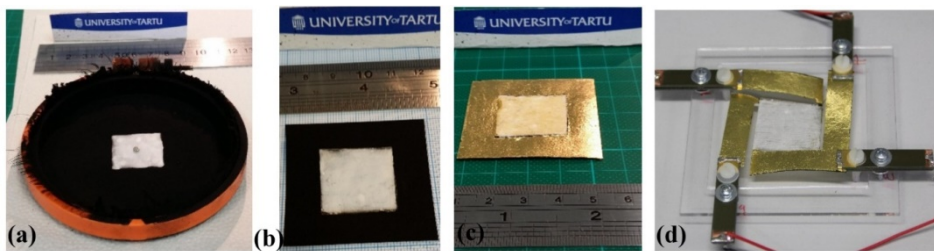

Figure 18. Photographs of the fabrication process

5.4 Experimental setup and workspace analysis

Experiments are conducted to characterize and analyze the maximum work-space (displacement and rotation angle) and the blocking force of the proposed motion system. The experimental arrangement and its schematics are shown in Figure 19(a) and 19(b). Three infrared analog distance sensors (SHARP GP2Y0A51SK0F) are fixed below the platform and the position data is used to construct a 3D surface in real time. Four additional sensors (SHARP GP2Y0A51SK0F) are fixed for each of the actuators to measure the tip displacement. Force transducers MLT0202 from AD Instruments with measurement range 0 - 0.245 N are used to measure the blocking force. The sensor data is collected using National Instruments PCI 6036E via an SC-2345 connector module. The actuators are driven via a National Instruments PCI 6703 data acquisition card and amplified by power op-amp LM675T via NI SCB-68 connector module. A computer running MATLAB/Simulink is used as a user interface to control the input and output through the sensors and actuators.
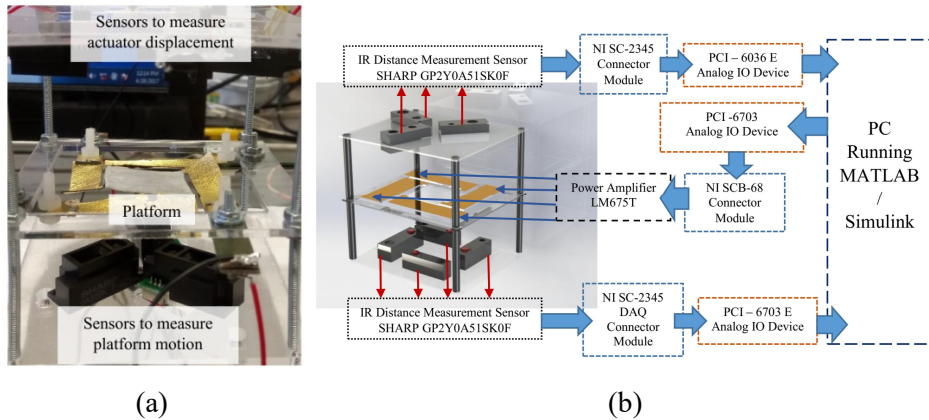
(a)	(b)

Figure 19. (a) Sensor arrangement (b) Schematics of the motion system electrical connection

To measure the workspace of the manipulator, the actuators are excited with a maximum step voltage of 2 V. Voltages above the maximum value will result in the electrolysis of water which is absorbed from the surrounding environment by the hydrophilic ionic liquid. Also, the high voltage causes heating effects resulting in the softening of the material that influences the actuator's stiffness causing unstable and undesirable platform motion. Further heating reduces the lifetime of the actuator.

The positive polarity of the input voltage causes the actuator to move up along the Z axis and the negative polarity causes downward motion. Different combination of voltage polarity to each of the actuators causes the system to produce different degrees of motion and the results are shown in Figure 20(a)-(f).
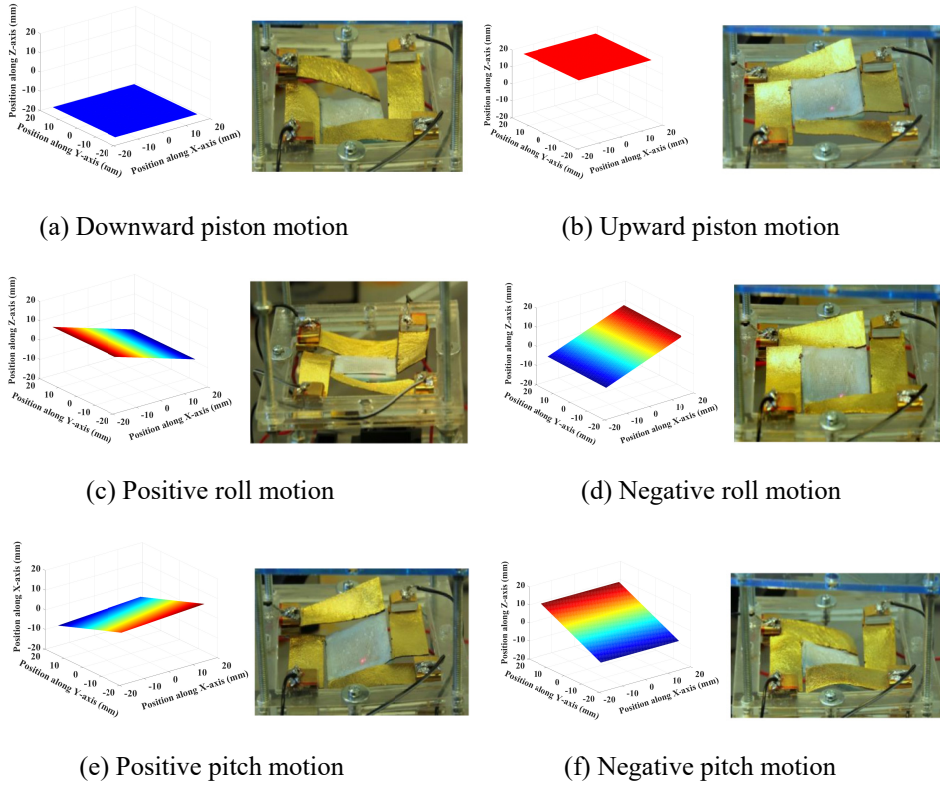
(a) Downward piston motion

(b) Upward piston motion

(c) Positive roll motion

(d) Negative roll motion

(e) Positive pitch motion

(f) Negative pitch motion

Figure 20. Experimental results of the proposed mechanism

5.5 Results and discussion

The maximum displacement during upward and downward piston motion for the step voltage of 2 V is about ±15 mm, whereas the prediction made through simulation is ±16 mm and the rise time to reach 90% of the maximum displacement is about 18 *s*. The maximum angle reached during roll and pitch is about ±14.8 and ±15.5 degrees respectively, whereas ±18 degrees are obtained through simulation in both axes. Compared to linear motion, the discrepancies between experimental and simulation rotational strain and displacement are large and this is accounted to the glass slide fixed on the platform acting as a stiff payload and restricts rotation movements. The comparison between experimental and the simulation results are shown in Figure 21.
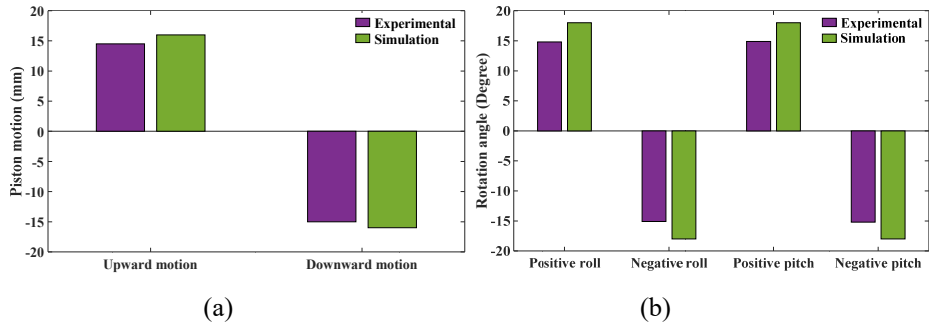
(a)   (b)

Figure 21. Comparison of simulation and experimental results

To study the frequency response of the actuator, it is excited with a sinusoidal input signal of 2 V with a frequency range from 0.01 to 0.4 Hz and the resulting displacement is shown in Figure 22. The maximum peak-to-peak displacement is saturated at 0.01 Hz and as the frequency of the input voltage increases, the displacement decreases and becomes negligible at 0.4 Hz as these devices are rate limited due to the slow ion transport process.

(a)

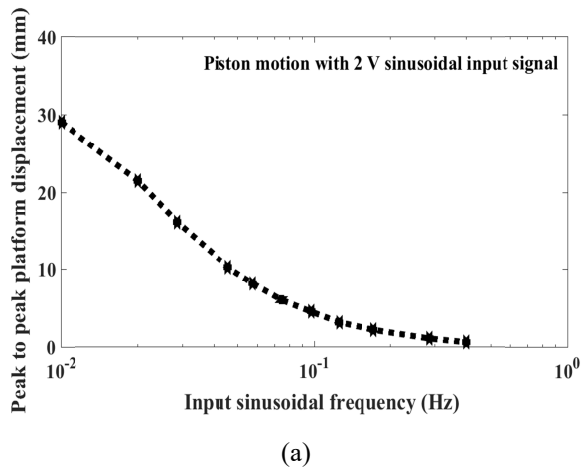**Figure 22**. Input frequency vs peak-to-peak displacement (mm)

5.5.1 Blocking force response

To measure the blocking force, the force transducer is placed such that the tip touches the center of the platform. On the application of potential, the movement of the actuator is restricted and rather applies force on to the transducer tip that is measured. The arrangement is shown in Figure 23(a). The

maximum force generated at the center of the platform actuated by four actuators is 1.6 mN and is shown in Figure 23(b).
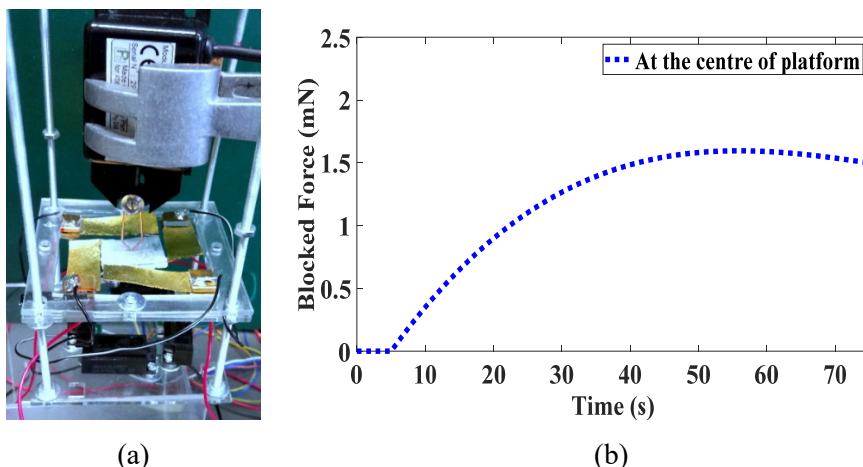

(a)   (b)

Figure 23. (a) Photograph of the force measurement arrangement (b) Force at the center of the platform

5.6 Limitation of the CPC manipulator

There are two main shortcomings encountered in the proposed system. The first one is in the fabrication method, the device is fabricated manually as described in this chapter which is a time-consuming and tedious process. Also, the manual spray coating method results in obtaining samples of non-uniform thickness along the length of the actuator and also thickness differences between each actuator results in a parasitic twisting motion of the platform. The second drawback is the very low speed of response of the actuator. Even though the system was able to obtain considerably large stroke and rotational angles, the operating frequency range is quite low. The slow response of the system is attributed to very thick electrodes (280 μm), which requires long charging time and also inherently carbon-based actuators are slower compared to other materials used for fabrication of IEAPs. Actuators with thin electrodes will respond faster but their low stiffness causes slagging of the center platform at rest and also the thin electrodes are not capable of carrying an additional payload for further experiments. Hence the present system as such can only be applied to a real-time application that operates only in a very low-frequency range.

In order to overcome the above drawbacks, we propose printing of the proposed configuration in a miniaturized version eliminating manual fabrication and also achieving batch fabrication. In order to adopt the device for the printing process, the carbon-based electrode is not found to be the right

candidate. Since the printing of carbon-based electrode needs further research and also inherently carbon-based actuators are slower in response compared to conducting polymer-based actuators. Hence, in order to obtain high-throughput production using commercially available materials and also to enhance the response speed of the manipulator, it is proposed to use poly(3,4-ethylenedioxythiophene):poly(styrenesulfonic acid) (PEDOT:PSS) conducting polymer for printing the configuration. Among several conducting polymers, PEDOT:PSS is considered as one of the most successful ones and is widely available commercially owing to its properties such as high conductivity, high flexibility, and excellent thermal stability [53]. Also, the printing of PEDOT:PSS is well-studied [9,54–57] and also this polymer is commercially available. With these advantages, the device is printed using PEDOT:PSS electrode over a PVdF separator membrane. The methods, materials and the characterization of the printed manipulator are explained in the next section.

6. PRINTING OF CP SOFT PARALLEL MANIPULATOR

In this section, fabrication of the proposed manipulator using PEDOT:PSS as the electrode material using an additive manufacturing technique including a syringe-type printer is discussed. In general, common techniques for fabricating conducting polymer ionic soft actuators include direct electrochemical synthesis [58,59], spin coating [60] and drop casting [61,62]. For the fabrication of micro-devices and lab-on-a-chip applications, these techniques are combined with microfabrication and photolithography techniques [3,63]. However, this requires a cleanroom facility and is also both a time-consuming and expensive approach. Recently inkjet and syringe-based printing of conducting polymer actuators have been reported [54,55,57,64]. Compared to cleanroom fabrication, these printing techniques are of low cost, little time consuming, and high precision and can be used in linear arrays for high throughput fabrication. Further, it allows the use of several materials in parallel that could be employed in the one-step fabrication of the actuators and sensors [57].

Printing PEDOT:PSS actuators with commercially available inkjet nozzle is highly challenging since it requires appropriate viscosity, density and surface tension [65,66] and there are issues involving low solubility and miscibility of conducting polymers. Various additives are often needed in order to adjust the rheological properties of the ink to make it suitable for printing with the inkjet nozzle [57]. On the other hand, the use of low-cost custom printing based on a syringe-type extrusion system provides a lot of freedom in terms of the use of various materials and the possibility to modify the printer to suit specific applications [67]. These types of printers use a bottom-up manufacturing technique where the material is added layer-by-layer on a substrate or device and can achieve (soft robotic) structures which are difficult or impossible to produce with more traditional manufacturing techniques. This method allows for easy fabrication of soft robotic devices using commercially available off-the-shelf materials with limited or no chemical processing [67].

6.1 Fabrication of the proposed configuration

The ionic manipulator is fabricated using printing/additive manufacturing where the actuator is built by adding layers to replicate a digital 3D-model. The printer and its schematics are shown in Figure 24(a) and 24(b). For the current work, the digital 3D model is designed using Solidworks (Dassault Systems); and Seraph studio software is used as a slicer tool to generate g-code instructions for the printer. A batch of printed actuator arrays is shown in Figure 24(c).
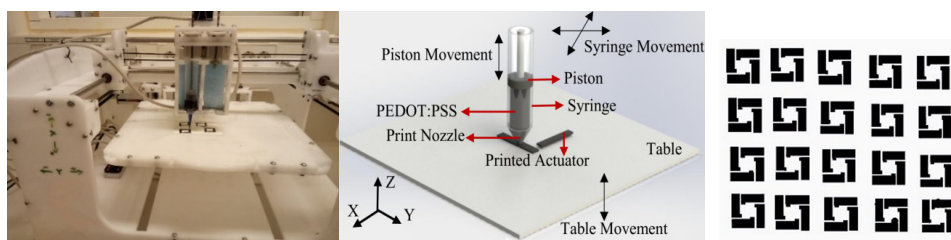
Figure 24. (a) 3D-printer photograph, (b) printer schematics, (c) batch of the printed matrix array

An aqueous dispersion of PEDOT:PSS (Clevios TM PEDOT:PSS ink PH1000, Heraeus GmbH) was used as the electrode material for printing the actuator segments of the manipulator, and the syringe containing the solution acts as the deposition tool or the extrusion system. In order to increase the conductivity, 5% w/w Dimethyl sulfoxide (DMSO) is added [42]. The content was mixed together and stored in the 10 ml syringe with an extraction nozzle diameter of 400 μm. The deposition tool can translate in the x and y-directions (horizontal plane) while the material is deposited by the movement of the piston in the syringe. To create multi-layered structures, either the table or the deposition tool can be moved in the z-direction, creating space for depositing the next layer. The rate of deposition is controlled by controlling the pressure on the piston and by the nozzle translation speed. By adjusting these parameters, the syringe-based printers can be made to extrude both high and low viscosity material.

Commercially available PVdF membrane (IPVH00010 by Immobilon) with 125 μm thickness is used as the separator membrane onto which the electrodes are printed. The membrane is hydrophobic in nature and hence it is oxygen plasma treated (200 W power for 5 min) before printing to make the surface hydrophilic. Once one side of the membrane is printed, the electrode is dried at 40 ^{0}C for 6 hours before resuming to print on the other side.

Once the PEDOT:PSS electrodes are printed on both sides of the membrane, 1-ethyl-3-methylimidazolium bis(trifluoromethylsulfonyl)imide (EMIM-TFSI from Sigma Aldrich) ionic liquid is dropped on top of the printed material and it is kept between 2 glass slides for 12 hours. Before characterization, the sample is sliced using a scalpel appropriately removing the unwanted membrane region and thus freeing the actuators from platform resulting in the parallel manipulator. The schematics of the fabrication process are shown in Figure 25(a). One layer of PEDOT:PSS is printed on both sides of the membrane resulting in an electrode thickness of 15 μm on each side, and the dimension of each actuator is 11 mm in length and 4 mm in width. The dimensions of the entire manipulator with the central platform and four actuators are 16 mm × 16 mm. The SEM micrograph image showing the printed actuator cross-section with a single layer of the electrode on both sides of the PVdF membrane is shown in Figure 25(b).
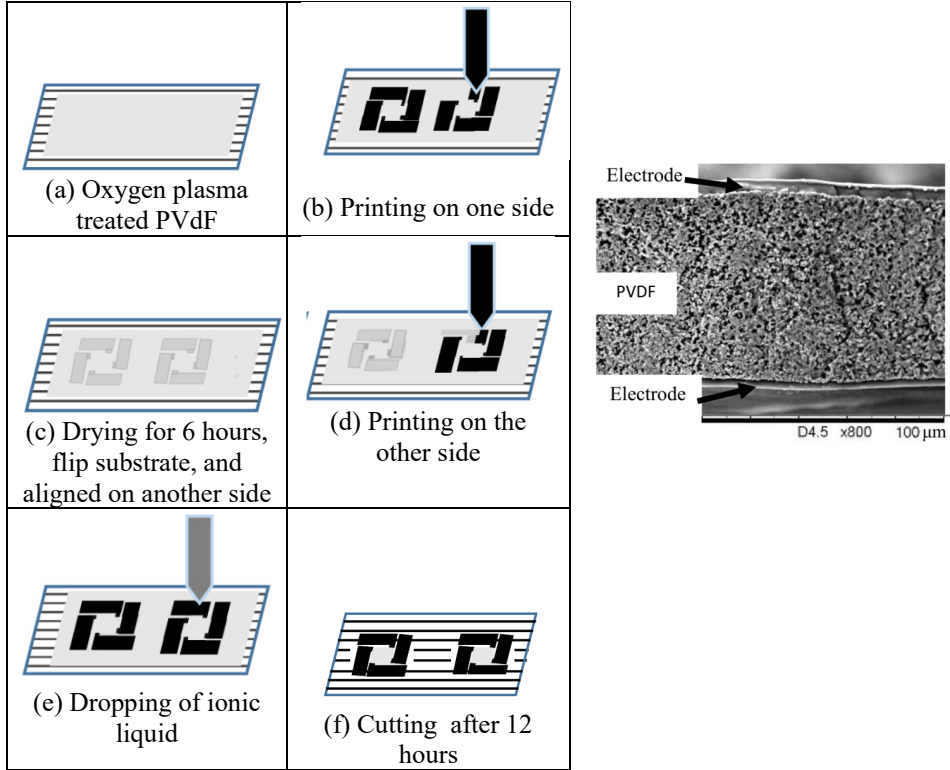
Figure 25. (a) Schematics of the fabrication process (b) SEM image of the printed sample

6.2 Modelling, experimental setup and workspace analysis

The printed actuators and the assembly of the device are shown in Figure 26(a) and 26 (b). Due to the limited space in the arrangement, the three position sensors used for measurement in CPC actuators are removed and the much simpler measurement method is adopted to measure rotational and linear motion has shown in Figure 27. A gold sputter-coated mirror is fixed on to the platform and is used to steer a laser beam from a laser displacement sensor (LG10A65PU) on to a calibrated measurement scale. The reflected light is used to calculate the rotational angles using the Eq. 31. To measure the workspace of the manipulator, the actuators are excited with a maximum step voltage of 2 V with a different combination of polarity. The schematic arrangement of the experimental setup is shown in Figure 27a. To measure the linear motion, a laser displacement sensor is used directly without the mirror.

$$\theta = \sin^{-1}\left(\frac{L1}{\sqrt{L^2+L1^2}}\right).$$ (31)
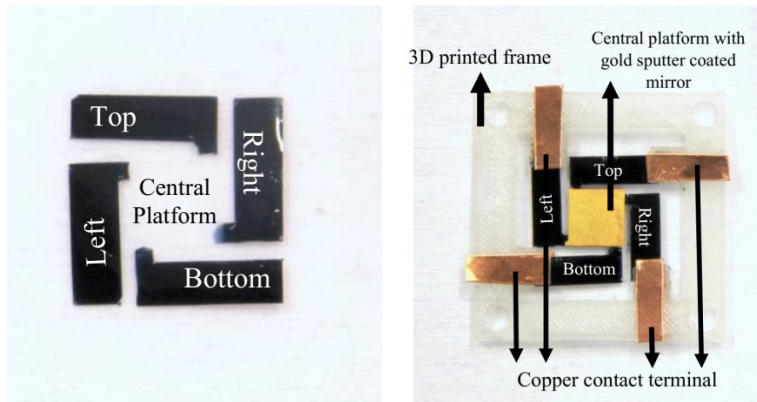
Figure 26. (a) Printed manipulator with the central platform and four actuators (b) Manipulator fixed to the frame with electrical connection with a gold sputter coated mirror fixed to the platform
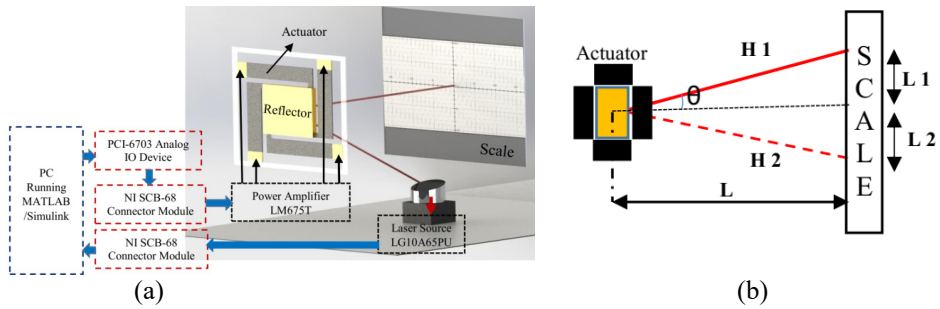

Figure 27. (a) Schematics of the experimental setup with input/output DAQ channels connected to the actuator and platform reflecting light on to the scale (b) Angle measurement schematics with laser light reflected on the scale at a rotational angle of θ.
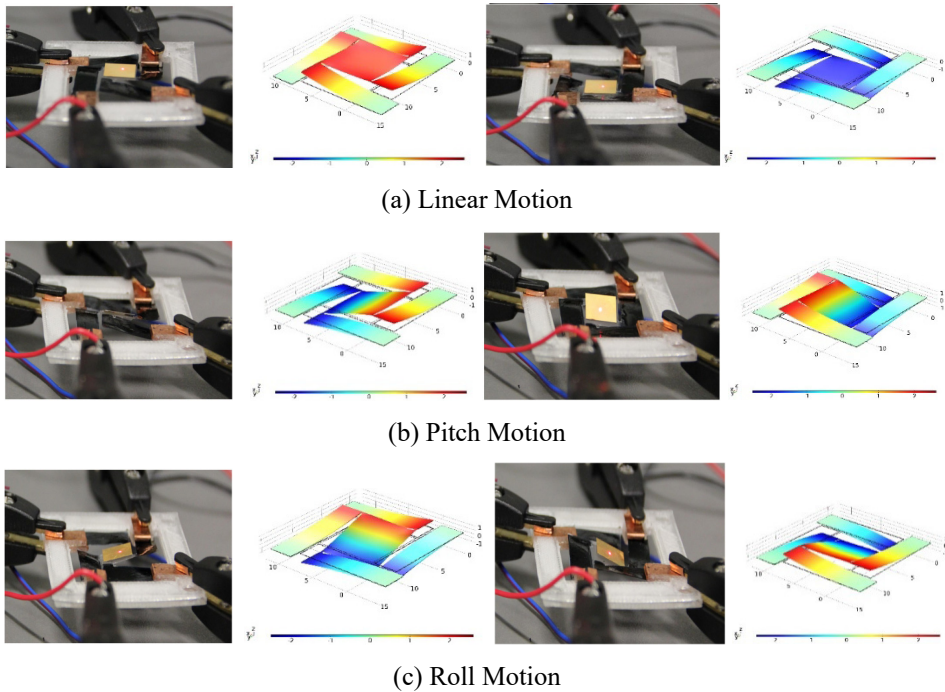
(a) Linear Motion

(b) Pitch Motion

(c) Roll Motion

Figure 28. Displacement and rotational movement of the fabricated manipulator and comparison with simulation results. (a) Linear motion showing maximum and minimum positions, (b) Pitch motion in both extreme rotational angles (c) Roll motion in both extreme rotational angles

The photographs of the maximum linear movement and rotational motion along the different axes compared with the simulation models are shown in Figure 28. The maximum tip to tip linear displacement achieved by the platform is 5.1 mm and the overall rotation angle along the x-axis is 11.36° and along the y-axis is 11.12°.

To measure the rise time and the frequency response of the manipulator, square wave and sinusoidal potentials were applied and the linear displacement of the platform was measured using a laser displacement sensor. With the square wave potential of 0.1 Hz and +2 V to -2 V the platform displaced from -2.5 mm to 2.6 mm resulting in a total peak to peak displacement of 5.1 mm. The rise time of the platform to reach 90% of its maximum displacement from the neutral position is 0.27 s and the response is shown in Figure 29(a). For the frequency response measurement, the 2 V sinusoidal input signal is applied to the actuator with frequency ranging from 0.1 Hz to 12 Hz. The peak-to-peak displacement is about 5.1 mm at 0.1 Hz and progressively decreases as the frequency increases and becomes negligible at 12 Hz as these devices are rate-limited due to the slow ion transport process [63]. The frequency response is shown in Figure 29(b).
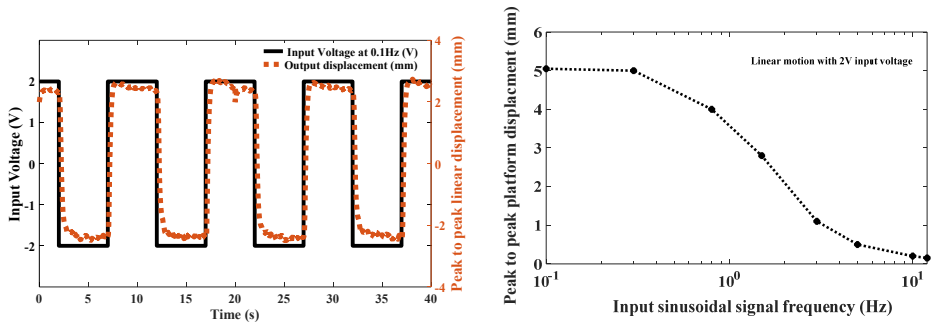
Figure 29. (a) Input voltage of 2 V square wave signal and output linear displacement of the actuator at 0.1 Hz (b) Frequency Response of peak-to-peak displacement from 0.1 Hz to 12 Hz
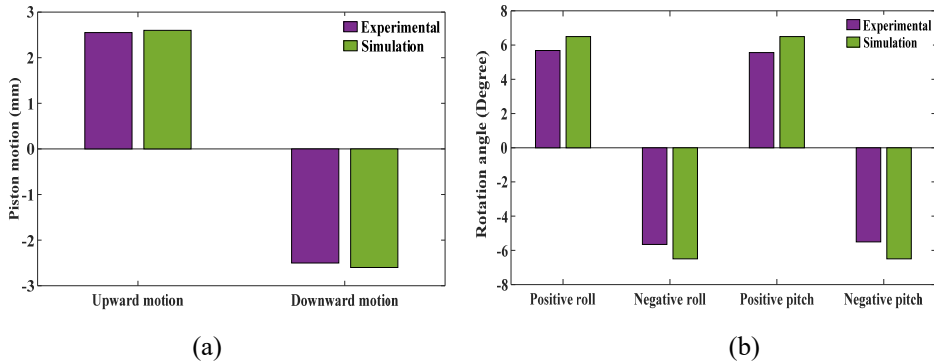
Figure 30. Comparison of simulation and experimental results (a) Comparison between experimental and simulation for linear displacements (b) Comparison between experimental and simulation for rotational angles

The comparison between the experimental and simulation values are shown in Figure 30. The linear peak-to-peak piston motion from the simulation results predicts a displacement of 5.2 mm which is very close to the measured experimental value of 5.1 mm with a percentage error of 1.92% showing good agreement with the developed model. In the case of the rotational angles, the predicted values through simulation are 12.4° on both axis, whereas the experimental values are 11.12° and 11.3°. The maximum error percentage is 10.3%, the increase in error is assumed due to additional torsional forces acting on the joints between platform and actuators which are not included in the model during simulation. Nevertheless, the maximum error between the experimental and simulation results is about 10% which is sufficient to characterize, visualize, design and optimize the system before fabrication.

6.2.1 Blocking force response

The experimental arrangement of the force measurement setup positioned at the center of the platform is shown in Figure 31 **(a)**. For the applied 2 V step voltage signal, the maximum blocking force generated by the manipulator is 0.6 mN.

(a)   (b)

Figure 31. (a) Photograph of the force measurement setup (b) Force response for step input voltage with a maximum force of 0.6 mN

6.3 Comparison of CPC and CP soft manipulator performance
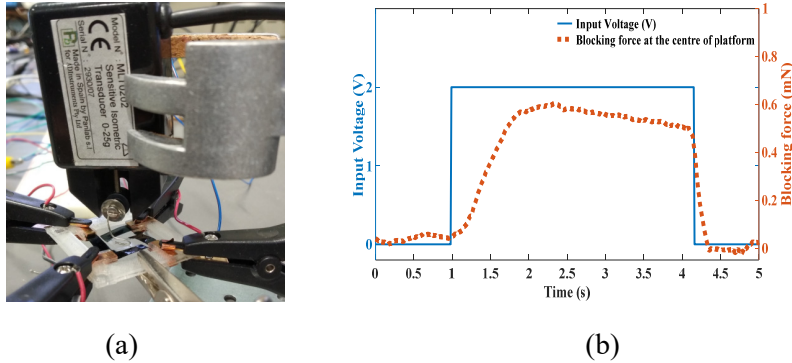

(a)   (b)
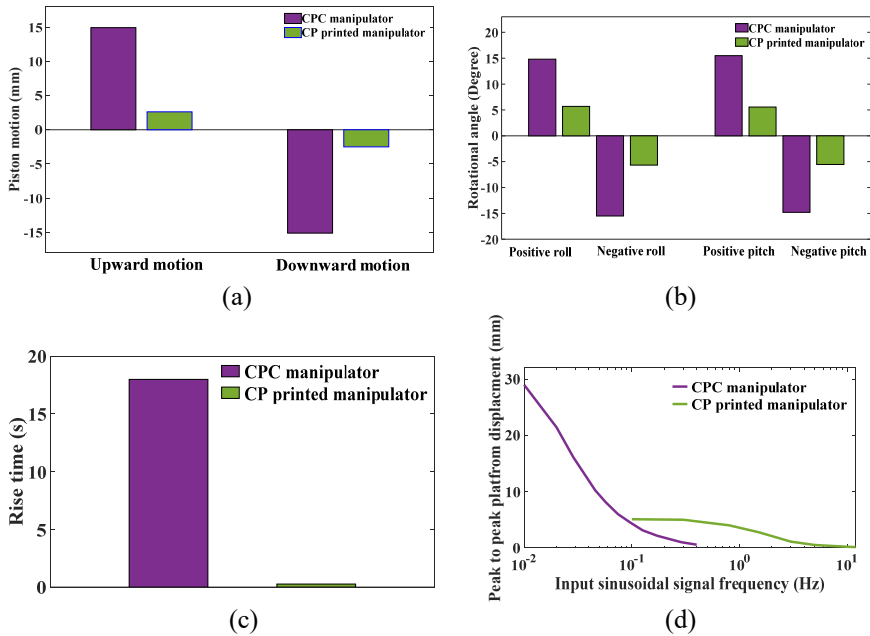
(c)   (d)

Figure 32. Comparison of CPC and PEDOT:PSS manipulator (a) Piston motion (b) Rotational motion (c) Rise time (d) Frequency response

The comparison between the carbon-polymer-composite manipulator and the printed PEDOT:PSS manipulator is shown in Figures 32 (a-d). But the size scale of the manipulators are in a different order, the area of the CPC manipulator with each actuator length of 40 mm and width 10 mm is 53 x 53 mm^2 with a 3 mm gap between the actuator and the platform, whereas that of CP is 16 mm x 16 mm with actuator dimension 11 mm length and 4 mm width. Hence to legitimately compare the three degrees of motion, the ratio of the maximum displacement to the length of the actuator is compared. From Figure 33, L_1 is the length of the actuator and L_2 is the pitch displacement. For a CPC actuator with length 40 mm and ±15 mm pitch displacement, the ratio of pitch to length is ±0.375, whereas the piston displacement to length ratio of a CP manipulator is 0.236. Similarly comparing the ratio of rotation angle with respect to the length the ratio is ±0.387 for CPC and 0.513 for CP manipulator. The linear displacement of CPC is considerably better than that of CP whereas the latter was better in terms of rotational angle generation. The main reason for limited rotational angle in the CPC manipulator is attributed to the microscope glass slide fixed on the membrane. The glass slide is essential to make the platform stable since the membrane and glass fiber alone will make it wrinkle during actuation. But this additional payload limits the maximum achievable motion. But considering the speed of response between the manipulator types, CPC had a rise time of 18 s, whereas PEDOT:PSS electrode provides a very quick response of 0.27 s. From the frequency response analysis, it can be seen that the CPC displacement almost becomes negligible at 0.4 Hz, while the CP manipulator response is measured till 12 Hz. Overall in comparison, CP-based manipulators have a faster response and also achieve comparable displacements and rotation angles. Further, the CP manipulator is nearly three times smaller in terms of overall surface area, making it very compact. Moreover, the additive manufacturing method is considerably less tedious and allows the possibility of batch fabrication for high throughput production.
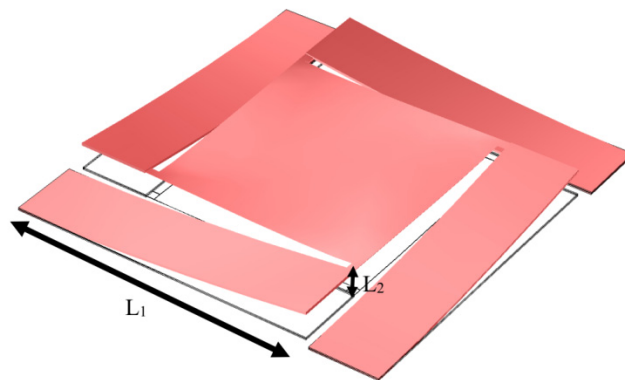

Figure 33. Parameters for the comparison ratio between manipulators.

7. APPLICATIONS

Ionic electroactive actuators with manipulation capability in one or two axes have been explored for application in several fields. An IPMC-based micro mirror developed by Yun *et al.* [68] consisting of two ring-shaped cantilever beams with a length of 8 mm was capable of producing motion along two axes generating a 0.25 mm linear displacement and the maximum tilting angle of $\pm$ 11.3° on one axis at an input voltage of 4 V. The tunable one axis gear shaped IPMC focusing mirror with three actuators with a circular mirror designed by Tsai *et al.* [69] was able to generate a maximum displacement of 45 μm and was capable of showing 77.8 m^{-1} optical power change which is a change in the reciprocal of the focal length of the device. The IPMC mirror-based optical zoom module for the compact camera developed by Chen *et al.* [70] was able to change the optical power to 73.8 m^{-1} with 3 V and attained a maximum displacement of 200 μm. With reference to linear actuating stage, Mutlu *et al.* [7] developed a spiral arrangement of the three-actuator configuration with polypyrrole actuators to be used as a microscope stage mechanism that was able to generate 1 mm displacement at 1 V. Yamakita *et al.* [71] proposed four IPMC actuator configuration with a flexible connector that generates the maximum displacement of 10 mm at 2.5 V. The linear actuator using carbon-based electrode for a mirror application developed by Torop *et al*. [72] was able to generate a stroke of 15 μm at 3V along lateral direction. The manipulator configuration developed in this work with PEDOT:PSS electrodes was able to generate a peak-to-peak linear stroke of about 5.1 mm, which is higher in comparison to other designs proposed earlier in the similar size scale [68–70,72]. Also, in comparison to the maximum tilting angle of 11.3° on one axis achieved earlier for a mirror application [68] the proposed configuration in this work was able to generate similar angles additionally it can move in two different axes. Overall in comparison, apart from achieving larger displacement, this configuration is capable of generating three degrees of freedom motion all in a single compliant mechanism. Moreover, the manipulator was completely fabricated using off the shelf commercially available materials along with the possibility of batch processing using additive manufacturing technique. With the consideration that angular motion more than 10° has a good advantage in the field of the display module and optical system [68], the current configuration is outstanding within the soft robotics system and has potential application in the above-discussed fields in addition to other applications such as a zoom lens, a microscope stage, laser steering, autofocusing systems, biomedical manipulators etc.

In order to demonstrate simple applications of the printed CP manipulator, four-way optical switch and a microscope stage application with closed-loop feedback control were designed and presented.

7.1 Optical switching and laser steering – open loop application

In order to demonstrate an open loop application of the proposed manipulator, a four-way optical switch was designed and characterized. The experimental arrangement consists of four light dependent resistors (LDR) fixed at a predetermined position (at the boundary of the workspace of the manipulator) as shown in Figure 34(a) and the electrical schematic of the LDR is shown in Figure 34(b). On the incident of light rays on to the surface of the resistor, the resistance changes causing a change in the potential which can be measured. This change in potential can be used as a switching action to trigger further actions/processes. The manipulator is fixed at a defined position and a laser beam is directed on to the mirror of the manipulator. The actuators are excited in an automated sequence such that the mirror steers the light from the laser on the surface of the LDR, triggering the switch action. By manipulating each of the actuators in the manipulator, the LDR's can be switched ON/OFF optically in the desired sequence. It is possible to have an array of LDR's within the workspace of the manipulator and trigger each resistor precisely by controlling the manipulator achieving a multiplexed optical switch. For the purpose of demonstration, in this experiment, only four LDR's are used. The input switching signal to the manipulator actuators is shown in Figure 35(a-d) and the LDR response and photographs of each switching action are shown in Figure 36(a-e) respectively.

(a)   (b)
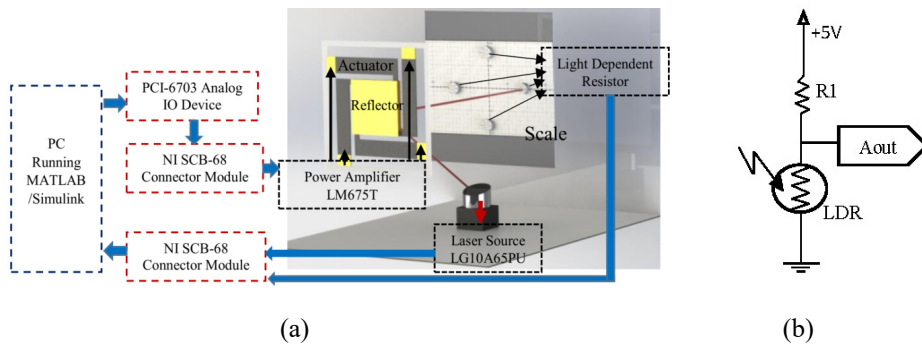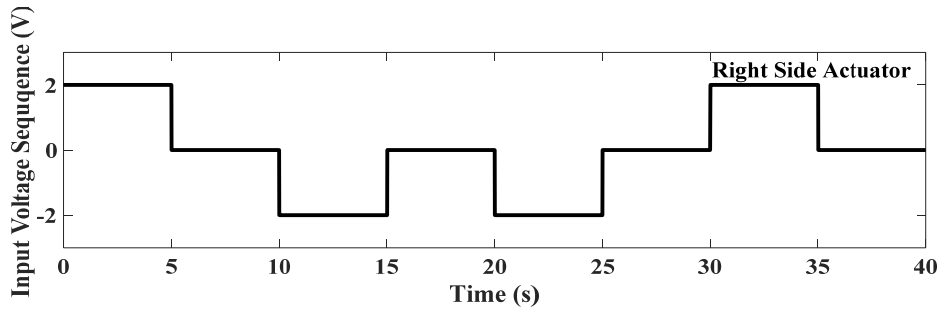
Figure 34. (a) Schematics of the optical switch application with input/output connection to the manipulator and LDR position at a predetermined position (b) LDR Sensor electrical connection for potential measurement
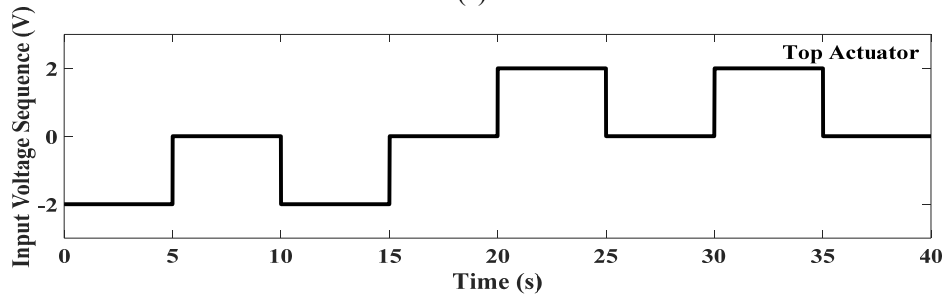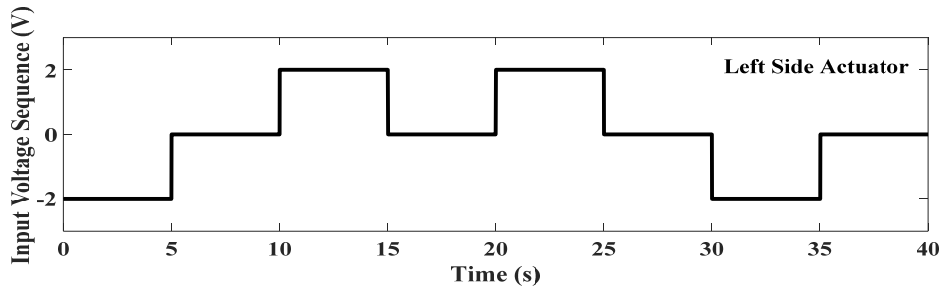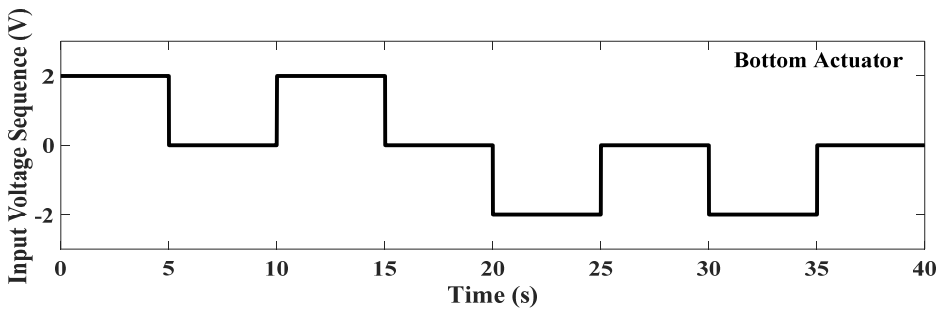
Figure 35. (a–d) Automated trigger signal sequence to the each of the actuators (denoted as top, right, bottom and left) of the manipulator.
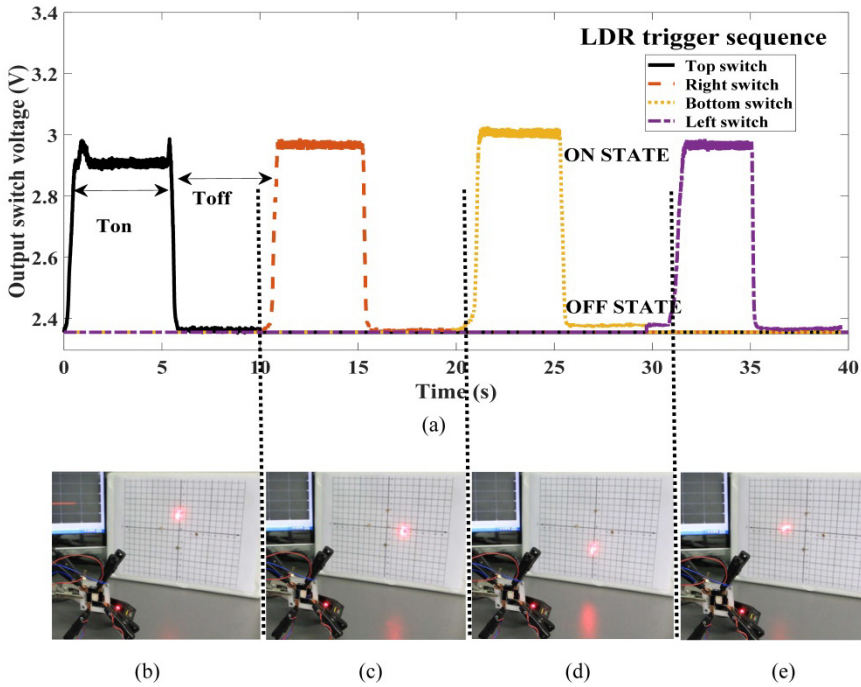
Figure 36. Optical switching of four LDR sensors in the xy-plane at the boundary of the workspace of the manipulator (a) The response of the four LDR switching from OFF state to ON state in accordance to the actuator switching sequence (b-e) Photographs showing the laser spot at the four positions switching the LDR.

The manipulator was able to achieve fast switching action with 0.84 s to trigger from a complete OFF state to ON state, of which 0.27 s is used to orient the manipulator from the rest to its new position. Apart from switching, the ability of the manipulator to steer light in the xy-plane also has other potential laser steering applications. This demonstration illustrates the ability of the monolithic flat printed actuators to manipulate in the xy-plane, which is a much simpler system as compared to two servo motors that are normally required for such applications.

7.2 Microscope stage – closed loop application

In this chapter, the development of a feedback controller of the CP printed soft manipulator for potential low-cost automatic microscope stage application is discussed. The device is used to move a specimen of interest into the field of view under the microscope accurately. Compared to the manual stage, the commercially available motorization hardware (motorized translators, controller boxes, etc.) are complex and often expensive [73]. To use the printed mani-

pulator as a microscope stage, closed loop feedback control is crucial since the specimen has to be positioned with precision within the focal point or field-of-view and also needs to be stabilized without oscillation. In the closed-loop feedback development, model building is an important step for the design of the controller. Most of the models proposed for ionic polymer transducers can be placed in one of three categories, physical models, black box models, and gray box models. In Chapter 4, a physics-based FEM model is used to describe the set of underlying mechanisms responsible for the electromechanical transduction. One difficulty with physical modelling is that the material parameters that appear in many of the governing equations do not lend themselves to direct measurement [74] to develop a feedback control model. Another issue with the physical model is that the governing equations are quite complex, hence much simpler models are needed for embedded controller implementation for application deployment [75]. In the case of a black box model based on the system identification method, the physical governing equation is discarded and only experimental data is used to fit a model. These models are best suitable for real-time controller implementation. One issue with the system identification method is the difficulty in finding the model structure and order of the model. However, Fang [75] developed a simple model structure reduced from a full infinite-dimensional physical model through model reduction, which captures essential actuation dynamics and is amenable to efficient real-time control. The developed model is a low-order transfer function model that is scalable and suitable for real-time control. Considering the current microscope stage application operated in the low-frequency range, the reduced order model is a good approximation for control implementation. The model structure obtained by ignoring high-frequency dynamics from an infinite-dimensional model is given in Eq.32

$$\frac{Output\ displacment}{Input\ voltage} = \frac{O(s)}{I(s)} = \frac{b_1 s + b_2}{s^2 + a_1 s + a_2} . \tag{32}$$

7.2.1 System Identification

To find the parameter in the model represented in Eq. 32, the system identification method of dynamic modelling is used. Experimental data is collected by applying the dynamic input signal to the actuators and the displacement of the platform is measured as output. An example of input and output signals used for the identification process is depicted in Figure 37(a). Overall 33072 data points with a sampling time of 0.01 s are collected. For estimation, the data is divided into two parts, the first part is used to determine the model and the second part is applied to validate the model. MATLAB-based system identification toolbox is used for the implementation of the identification procedure. The current process modelling is based on the prediction error estimation method which provides good estimation accuracy compared to other similar methods and is

computationally less expensive [76]. Ljung (1997) gives a more comprehensive description of this identification method [77]. Usually, a model with the fit percentage of above 90% is proved to be sufficient as a representation model [78]. The identified model is shown below with parameters b_1=0.1227, b_2=3.398, a_1=4.863 and a_2=8.932.

$$\frac{Output\ displacment}{Input\ voltage} = \frac{O(s)}{I(s)} = \frac{0.1227s+3.398}{s^2+4.863s+8.932}.$$

(33)

The identified model fit percentage is 93.52%, while the loss function and final prediction error (FPE) obtained are 0.0345 and 0.003310 respectively. The identified model output and the measured output are depicted in Figure 37(b). The estimated model matches the experimental data in the low-frequency range below 2 Hz which is the frequency range of interest. Despite being simple, it captures the dominant physics of the actuator within the actuation bandwidth. In general, the behavior of ionic actuators exhibits large bending angles that is predominantly non-linear, but in the current system, the actuators bending angles are limited physically due to the geometrical configuration of the platform. The platform can achieve only small displacements in the linear region since the motion of the actuator is limited mechanically by the connections to the vertex of the stage and hence the motion is limited to small displacement range. For the small displacements, the linear model identified allows the best fit with the experimental data. The comparison of the frequency response with measured and simulated output is shown in Figure 38.

(a)

(b)

(c)
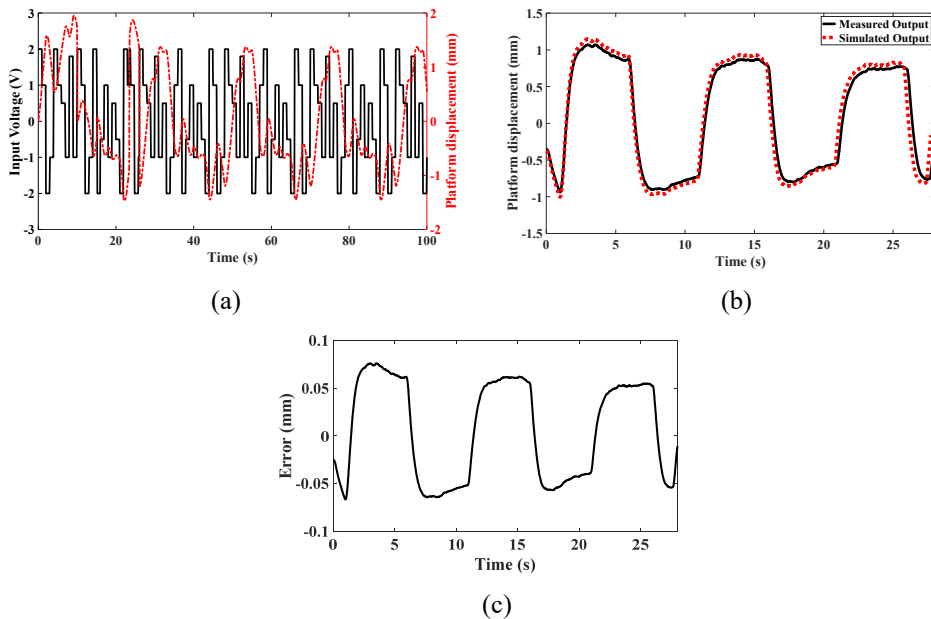
Figure 37. (a) Open loop input and output data (b) Model validation (c) Model error
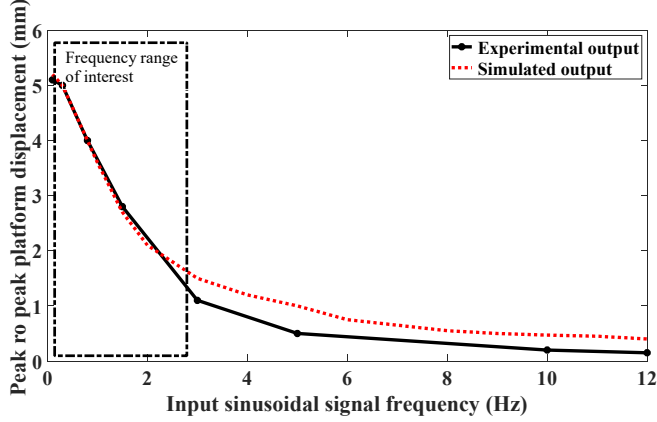
Figure 38. Frequency response comparison between experimental data and the simulation model

The above continuous time model is then converted to discrete time state space form for controller design and implementation on the real-time controller with sample time 0.01 s. The state space model is given by

$$x[n + 1] = Ax[n] + Bu[n]$$
$$y[n] = Cx[n] + Du[n] \tag{34}$$

$$A = \begin{bmatrix} -4.8630 & -8.9320 \\ 1 & 0 \end{bmatrix} \quad B = \begin{bmatrix} 1 \\ 0 \end{bmatrix} ,$$
$$C = [0.1227 \quad 3.3980] \qquad D = [0] \tag{35}$$

where x is the state vector, u is the input vector, y is the output vector, A is the state matrix, B is the input matrix, C is the output matrix and D is the feedthrough or feedforward matrix in case the system does not have a direct feedthrough ($D = 0$). Quite similar linear time invariant models and second order models for various applications and tip displacement control are reported for other ionic actuators by several authors [56,79–81].

7.2.2 Model predictive control

Model predictive control is a class of algorithms that compute a sequence of the manipulated variable/control signal in order to optimize the future behavior of the system. It is based upon solving an optimization problem for the control actions at each sampling interval [82]. The control method solves this optimization problem by using the current state of the actuator and the future predicted state from the model to obtain the optimal input vector [82]. In the MPC scheme, one considers the prediction of a system output over some prediction

time horizon N_H and aims to find a sequence of inputs and outputs over the prediction horizon [83].

MPC is ideal for multiple-input-multiple-output (MIMO) systems and is widely applied for microactuator applications where an array of actuators are functioning together [84]. Further, it can handle an uncertain system and is also supported with embedded constraints [85]. The main constraint while developing the controller for the manipulator is that the maximum voltage and rate at which it is applied to the actuator is to be limited so that they are operated within the electrochemical stability window to avoid electrolysis and overheating. Also, the maximum displacement of the actuator is limited in order to reduce the mechanical stress and ageing effect at large displacements.

Considering the above benefits and ease of designing and tuning made MPC is selected for the control of the microscope stage. The cost function or the optimal criteria used in the current controller is given by the following equation

$$J(K) = \sum_{l=1}^{N_H} [r(k+l) - y_m(k+l)]^2 + W \sum_{l=1}^{N_C} \Delta u^2(k+l-1), \qquad (36)$$

where

$$\Delta u^2(k+l-1) = u(k+l-1) - u(k+l-2),$$

Here, $r(k+l)$ denotes the prediction of the output at instant $k+l$ on the basis of information up to instant k (current time), $y_m(k+l)$ is a reference signal, $u(k+l)$ is the control signal and W are control weight factor respectively. Minimizing this objective function by a suitable choice of $u(k+l)$ will provide a trade-off between minimizing the tracking error of the system and increasing the amplitude of the input signal. The constraints which limit the range of the control signal, gradient of the control signal and the future model predictions are

$$u_{min} \leq u(k+l) \leq u_{max}$$

$$|u(k+l) - u(k+l-1)| \leq \Delta u_{max}$$

$$r_{min} \leq r(k+l) \leq r_{max}, \qquad (37)$$

where u_{min} and u_{max} are minimum and the maximum input signals to the actuators r_{min} and r_{max} are the minimum and maximum output displacement. Δu_{max} is the gradient of the control signal between two consecutive sample times.

Here the future outputs from the actuator are given by $y(k+l), l = 1,2,..N_H,$ where N_H is the prediction horizon up to which the future output

displacement is predicted from the model. The future output depends on the actuator's current states and future control signals. $u(k + l), l = 1,2,.., N_C$, where N_C is the control horizon parameter up to which future control signals are predicted. The predictive controller computes the potential future control signals such that the future outputs will be as close as possible to the desired position $r(k + l), l = 1,2, ..., N_H$ or in other terms the controller will compute the control signal such that it reduces the error to zero.
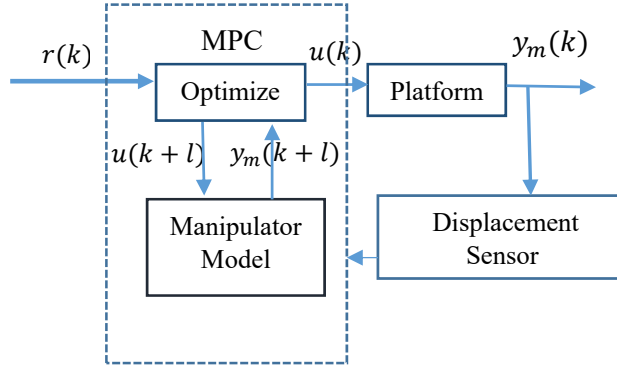
Figure 39. Control system architecture

7.2.3. MPC Tuning

For successful implementation, MPC parameters need to be tuned. The first parameter to be chosen is the prediction horizon N_H. This is commonly taken as at least 1.2 times the settling time of the system [86] and always $N_C \leq N_H$. Here the prediction horizon of 40 steps with 0.01 s sampling time is selected. The control horizon parameter $N_C = 10$ is tuned online for a smooth control performance, whereas $N_C >10$ only gives marginal performance improvements. The maximum and minimum control input signal is constrained to $-1.8\,V \leq u \leq +1.8\,V$. The set point or the displacement range is limited to $-1.5\,mm \leq y_m \leq 1.5\,mm$. Here, W is the tuning parameter which is tuned experimentally to obtain the desired performance. Table 4 represents the control parameters.

Table 4. Control parameters

Parameter	Symbol	Value
Sample time	t_s	0.1 s
Prediction horizon	N_H	40 (= 4 s)
Control horizon	N_c	10 (= 1 s)
Tuning weights	W	0.835

7.2.4 Experimental results: reference tracking control

Experiments are conducted to examine the performance of the designed controller and model for tracking/regulatory control of the manipulator. Position control by means of trajectory tracking experiments is conducted along the z-axis exhibiting linear motion. Different reference trajectories such as sine, square, sawtooth and staircase are used as test signals and the obtained results are depicted in Figures 40–43 along with the control voltages and error respectively. For tracking control, the controller optimally applies the maximum voltage of about 1.8 V without crossing the constraints. The maximum displacements for the reference are limited to 3 mm peak-to-peak. Figure 43 shows the tracking control of multistep staircase signals. The minimum resolution that the manipulator can track without introducing considerable noise from the IR sensor is 0.1 mm. The voltage applied for the staircase signal is shown in Figure 43(b). The results depict that the controller was capable of high precision tracking of the manipulator with 0.1 mm resolution in the range of +1.5 mm to -1.5 mm.

(a)   (b)   (c)
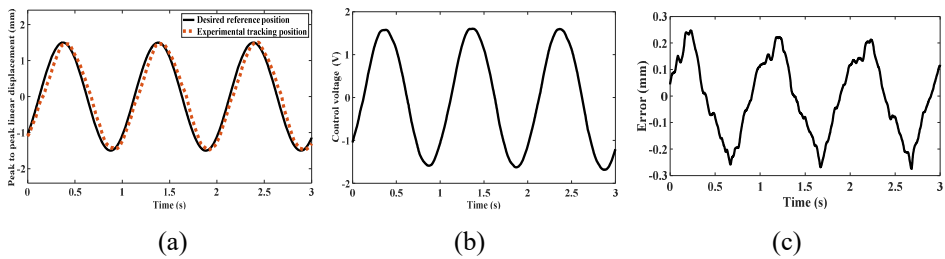
Figure 40. (a) Sine trajectory tracking (**b**) Controller output voltage (c) Error

(a)   (b)   (c)
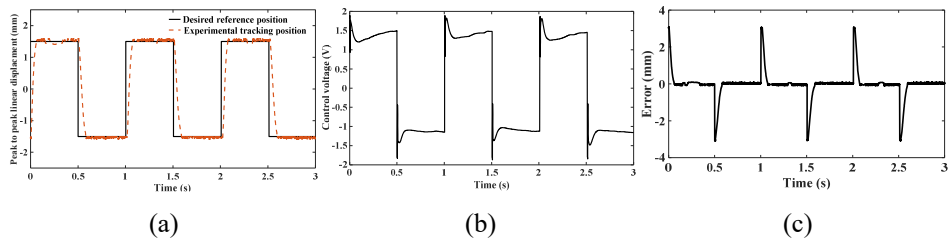
Figure 41. (a) Square trajectory tracking (**b**) Controller output voltage (c) Error

(a)   (b)   (c)
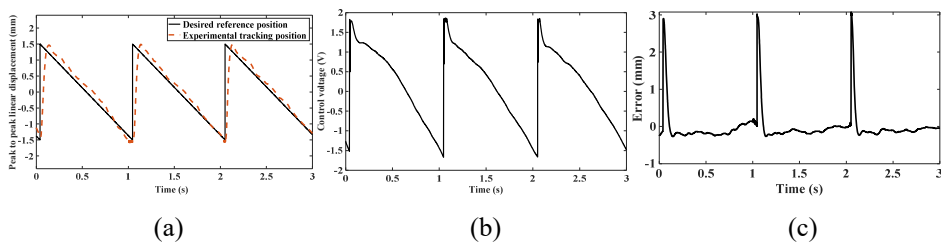
Figure 42. (a) Saw tooth trajectory tracking (b) Controller output voltage (c) Error

| (a) | (b) | (c) |
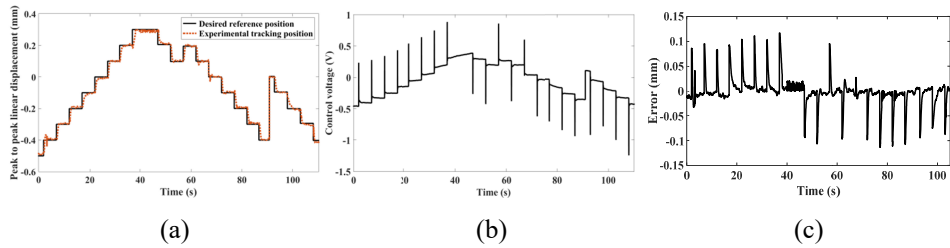
Figure 43. (a) Multistep trajectory tracking **(b)** Controller output voltage **(c)** Error

7.2.5 Real-time demo

The experimental arrangement for the application of the 3D printed microscope stage demo is shown in Figure 44(a). The comparison between a commercially available passive stage and 3D printed active stage is shown in Figure 44(b). During operation of the present 3D printed manipulator, a joystick is used to provide the desired reference signal to control the position of the stage under the microscope. The user can use the joystick to move the stage according to preference. A specimen of commonly found *Musca domestica* (Housefly) is used as a subject of interest and is shown in Figure 45(a). The entire length of the specimen is 6 mm and it is placed on the stage as shown in Figure 45(b).

The signal from the joystick is used as a reference signal to the controller and the controller applies the input voltage to the actuators to move the platform and thereby to move the specimen. An experiment is conducted to focus on a different region of interest of the specimen under the microscope using the joystick. Figure 46(a) shows the user input signal and the actuator following the reference trajectory and the control signal to the manipulator during the manipulation is shown in Figure 46(b). Figures 46 (a–d) show the results of the specimen under the microscope focusing the features of interest. Specific features such as the PVdF platform is focused and is shown in Figure 47(a), hair follicles in the midsection under investigation is shown in Figure 47(b), tips of the legs and the mouth and eyes section as depicted in the Figures 47(a) and (d) respectively. It is clearly seen that the 3D printed active stage can be precisely controlled as a microscope stage demonstrating the potential application.
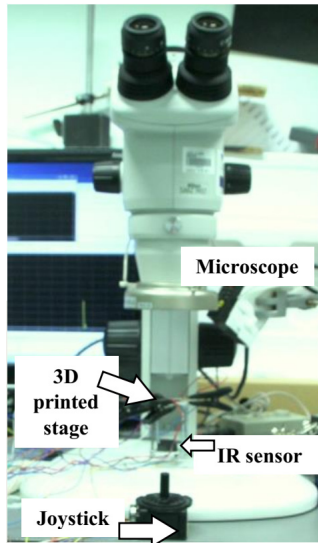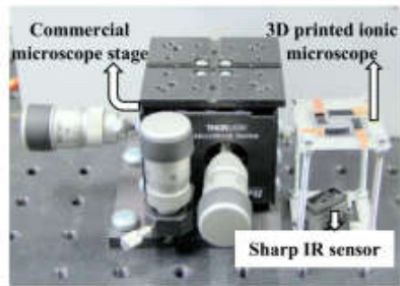
(a)   (b)

Figure 44. (a) Microscope stage experimental arrangement (b) Comparison of commercial stage and printed manipulator
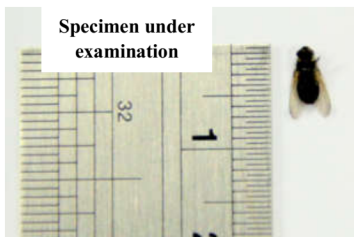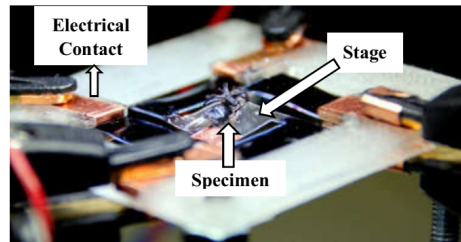
(a)   (b)

Figure 45. (a) The specimen under observation (b) Specimen placed on the stage
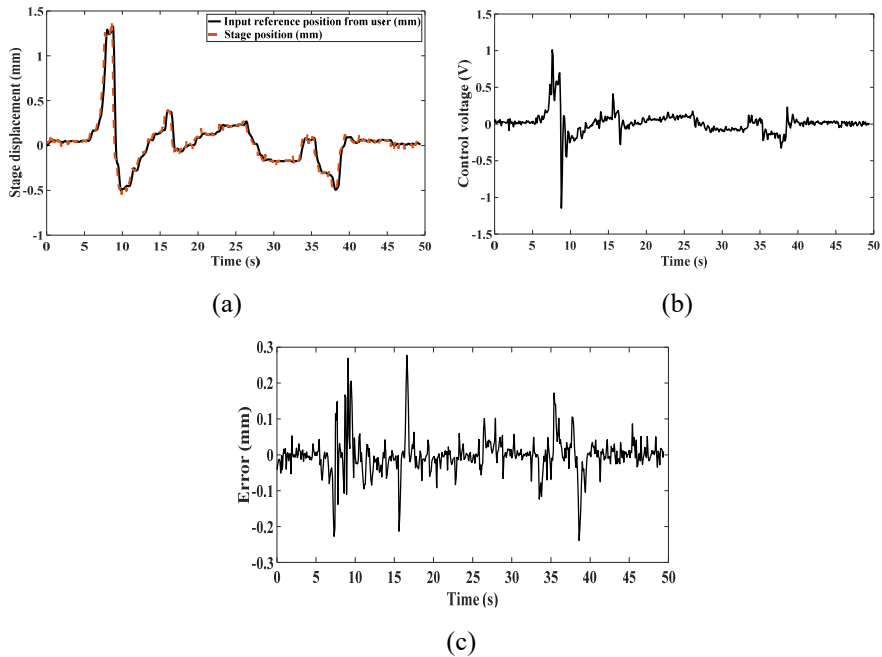
Figure 46. (a) User reference input from joystick and stage position in real time (b) Control input voltage (c) Error
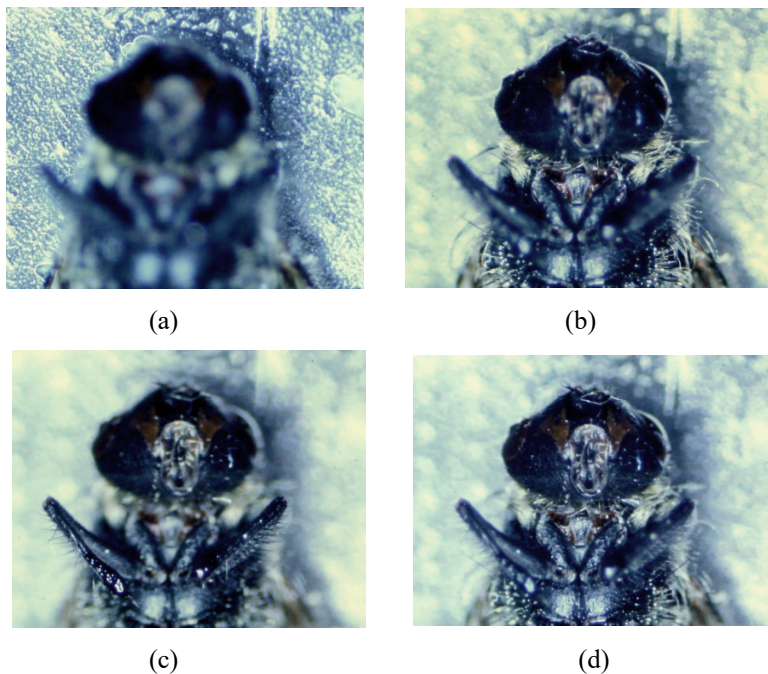
Figure 47. Focusing the features of interest (a) PVdF platform (b) Midsection hair follicles (c) legs (d) Mouth and head section

8. CONCLUSIONS

The future of soft robotic actuation systems with ionic electroactive polymer actuators is very promising especially in the microdomain for cutting edge applications such as micromanipulation systems, medical devices with higher dexterity, soft catheters with built-in actuation, bio-inspired robotics with better-mimicking properties and active compliant micromechanisms. However, still, there are significant challenges in understanding the transduction, developing simpler fabrication approaches and robust control schemes for real-time control. In this dissertation, an electro-chemo-mechanical model is provided with the emphasis of the charge storage mechanism in the ionic polymer actuator. The model is extended to design and structurally optimize the performance of the actuator through computer simulations before the fabrication process. A simple additive manufacturing method is presented for the actuator fabrication using low-cost syringe type printer that is a much more promising alternative to other known fabrication methods. The printing method allows to fabricate multipart and intricate patterns with high throughput production capability and also opens the opportunity to print a matrix array of identical actuators over a wide size scale.

In specific, the model presented in this work addresses the background electrochemical kinetics responsible for mass and charge transport process specific to the type of electrode materials and also provides insights in understanding the influence of physical properties of electrodes such as porosity and tortuosity on the electrical conductivity and deformation of the actuator. In addition, the model can deduce mechanical deformation direction and rate of deformation dependence on the mobility of the ions. For validation, simulations are conducted and the outcomes are compared with the experimental data. The results show that the model developed is able to well predict the behavior of the actuator, providing a comprehensive understanding of charge dynamics in the ionic polymer actuator.

The high fidelity of the model provides the opportunity to design, simulate and optimize complex ionic polymer actuator patterns and soft robotic systems, and as a result, a soft parallel manipulation system with three degrees of motion capability is designed and simulated. The developed system was manipulated by four independently controllable ionic polymer actuators and was capable of moving in 3 degrees of freedom, i.e. rotating around two axes (pitch and roll) and linear displacement along one axis. With satisfactory large displacements and rotation angles predicted from the model, fabrication of the device proceeds to the printing of the manipulation system. The results showed rotation angles of 11.36 degrees on two axes and 5.1 mm linear displacement along one axis with 0.27 s rise time. The obtained results show a close match with the simulation outcomes representing high fidelity of the model. Also, the performance of the printed manipulator is better than the CDC based manipulator which is fabricated using the tedious spray painting technique. In

considering the larger linear and angular motion with three degrees of motion and high speed of response, the printed manipulator produces higher displacement and rotation angles compared to previous devices that are fabricated directly using commercially available materials.

As a potential applications, a four-way optical switch and a microscope stage with feedback control using the printed CP actuator was demonstrated showing the capability of the parallel manipulation system. The four-way switch can optically trigger four light-dependent resistors in the xy-plane in an automated sequence, illustrating the ability of the monolithic flat printed actuators to manipulate in the xy-plane, which is a much simpler system as compared to two servo motors that are normally required for such applications.

For the microscope stage, model predictive control is developed for positioning and stabilizing the manipulator in the field of view under the microscope. It is shown that the MPC acts as a robust control scheme for deploying real-time applications that can foresee the constraints of the ionic actuators. The controller can also be extended to handle the uncertainties exhibited by the actuator due to changing environmental conditions. It is shown experimentally that the developed controller was well capable of predicting and controlling the actuator for micromanipulation applications with precision control. Overall this work results in modelling, fabrication, and real-time control of ionic electroactive polymer actuators leading to the development of a low-cost, monolithic, flat, multi-DOF parallel manipulator for micromanipulation.

The future direction of the work is to integrate a strain sensor as a part of the monolithic structure merged with printed electronics and onboard closed-loop controller to control each of the actuators of the parallel manipulator to make a fully autonomous motion system.

9. SUMMARY

Ionic electroactive polymers (IEAPs) based actuators are kind of smart composite materials that have the ability to convert electrical energy into mechanical energy. The actuators fabricated using IEAP materials will benefit from attractive features such as high compliance, lightweight, large strain, low voltage, biocompatibility, high force to weight ratio, and ability to operate in an aqueous environment as well as in open air. The future of soft robotic actuation systems with IEAP actuators is very promising especially in the microdomain for cutting edge applications such as micromanipulation systems, medical devices with higher dexterity, soft catheters with built-in actuation, bio-inspired robotics with better-mimicking properties and active compliant micromechanisms.

This dissertation has introduced an effective modelling framework representing the complex electro-chemo-mechanical dynamics that can predict the electromechanical transduction in this kind of actuators. The model describes the ion transport dynamics under electric field by combining the Nernst-Planck and Poisson's equation and the mechanical response is associated with the volumetric swelling caused by resulting charge and mass balance. The framework of this modelling method to predict the behavior of the actuator enabled to design, simulate and optimize compliant mechanism using IEAP actuators.

As a result, a novel parallel manipulator with three degrees of freedom was modelled and fabricated with two different types of electrode materials and is characterized and compared with the simulation model. It is shown that the developed model was able to predict the behavior of the manipulator with a good agreement ensuring the high fidelity of the modelling framework.

In the fabrication process, it is found that the manipulator fabricated through an additive manufacturing method allows to fabricate multipart and intricate patterns with high throughput production capability and also opens up the opportunity to print a matrix array of identical actuators over a wide size scale along with improved performance.

Finally, to showcase the competence of the printed manipulator, two different control applications were demonstrated. At first, an open loop four-way optical switch showing the capability of optically triggering four switches in the xy- plane in an automated sequence is shown followed by closed-loop micromanipulation of an active microscope stage using the model predictive control system architecture is shown. The application of the manipulator can be extended to other potential applications such as a zoom lens, laser steering, autofocusing systems, and micromirror.

Overall this dissertation results in modelling, fabrication, and control of ionic electroactive polymer actuators leading to the development of a low cost, monolithic, flat, multi DOF parallel manipulator for micromanipulation application.

10. SUMMARY IN ESTONIAN

Ioonsete elektroaktiivsete täiturite elektromehaaniline modelleerimine ja juhtimine

Ioonsed elektroaktiivsed polümeerid e. tehislihased on polümeermaterjalid, mille oluline iseärasus on võime muuta elektrienergiat mehhaaniliseks energiaks. Elektroaktiivsetest polümeeridest valmistatud pehmetel täituritel on mitmed huvipakkuvad omadused, näiteks suur deformatsioon madala rakendatud pinge korral, märkimisväärne tekitatud jõud ja massi suhe ning võime töötada nii vesikeskkonnas kui õhus. Niisuguste täiturite kasutamine on paljutõotav eriti just miniatuursetes eluslodusest inspireeritud robootikarakendustes. Näiteks võib tuua aktiivsed mikro-manipulatsioonisüsteemid või isepainduvad pehmed kateetrid, mis on iseäranis nõutud meditsiinitehnoloogias.

Käesoleva väitekirja uurimissfääriks on sellistest materjalidest valmistatud täiturmehhanismide modelleerimine, valmistamine ja juhtimine, päädides sisuliselt ühes tükis valmistatud mitme vabadusastmega paralleelmanipulaatorite väljatöötamisega. Kasutades kompleksset füüsikalistel, elektrokeemilistel ning mehaanilistel alusteadmistel põhinevat mudelit, kirjeldatakse ja ennustatakse sellist tüüpi täiturmehhanismide elektrilise sisendi ja mehhaanilise väljundi vahelisi seoseid. Mudel kirjeldab ioonide transpordi dünaamikat elektriväljas, kombineerides Nernst-Plancki ja Poissoni võrrandeid. Mitmekihilise polümeermaterjali mehhaaniline käitumine on seotud laengu- ja massitasakaalu poolt põhjustatud eri kihtide erineva ruumilise paisumisega ja kahanemisega. Kõike seda kokku võttes ning rakendades numbrilist modelleerimist lõplike elementide meetodil saadakse kvantitatiivsed tulemused, mis suudavad prognoosida täiturmehhanismi käitumist ja võimaldavad projekteerida, simuleerida ja optimeerida ka neil täituritel põhinevaid keerulisemaid mehhanisme.

Koostatud mudeli valideerimiseks modelleeriti ja valmistati kaks tööpõhimõttelt sarnast, kuid erinevatel elektroaktiivsetel polümeermaterjalidel põhinevat ning eri metoodikatel valmistatud mitmest täiturist koosnevat mitme vabadusastmega mikromanipulaatorit. Väitekirjas demonstreeritakse, et koostatud mudel on suure täpsusega võimeline ennustama nii iga individuaalse täituri kui ka mõlema manipulaatori käitumist.

Demonstreerimaks piisksadestusprintimismeetodil valmistatud manipulaatori efektiivsust, kirjeldatakse kahte erinevat kontrollrakendust. Esmalt näidatakse tagasisidestamata kontrollitavat seadet, kus pööratakse nelja täituri abil peeglit, suunates laserikiirt xy-tasapinnas ettemääratud punktidele. Teiseks näidisrakenduseks on tagasisidestatud kontrollmetoodikaga juhitav mikroskoobi preparaadiliigutaja, mille abil saab preparaati nii tõsta-langetada kui ka pöörata.

Manipulaatorite valmistamise käigus leiti, et piisksadestusprintimise meetodi täpsus, jõudlus ja skaleeritavus võimaldavad suure tootlikkusega valmistada identseid keerulisi mitmeosalisi manipulaatoreid. See tulemus näitab ilmekalt uue tehnoloogia eeliseid traditsiooniliste valmistamisviiside ees.

11. APPENDIX

Table 2: Parameters used in the CPC simulation

Symbol	Quantity	Value	Units	Reference
L_e	Carbon electrode thickness	118	μm	measured
L_s	Separator thickness	42	μm	measured
aC	Specific capacitance	26	F/cm^3	[87].
C_{ini}	Initial concentration	1100	Mol/m^3	measured
D_i	Diffusion coefficient of cation	$1.324*10^{-9}$	m^2/s	[88]
D_i	Diffusion coefficient of anion	$0.994*10^{-9}$	m^2/s	[88]
ϵ_e	Porosity of electrodes	0.60	-	measured
ϵ_s	Porosity of separator	0.55	-	measured
ρ_e	Solid phase conductivity	50	mS/cm	[87]
τ_e	Tortuosity of electrode	1.79	-	measured
τ_s	Tortuosity of separator	1.34	-	measured
ρ_p	Density of ionic liquid	1385.9	Kg/m^3	[89]
μ	Dynamic viscosity of ionic liquid	42.936	mPa·s	[90]
E	Equivalent bending modulus of CPC	371	MPa	measured
M_s	Molar mass of ionic liquid	0.260	Kg/mol	[89]
β_{ss}	Coefficient of swelling	9.5e-5	m^3/kg	Fitting parameter

Table 3: Parameters used in the CP simulation

Symbol	Quantity	Value	Units	Reference
L_e	Electrode thickness	15	μm	Measured
L_s	Separator thickness	125	μm	Measured
C	Specific capacitance	154.58	F/g	Measured
C_{ini}	Initial concentration	1800	Mol/m^3	measured
R_e	Electrode resistance	19	Ω/cm^2	measured
R_i	Electrolyte resistance	29	Ω/cm^2	measured
D_i	Diffusion coefficient of cation	$4.7*10^{-11}$	m^2/s	[91]
D_i	Diffusion coefficient of anion	$2.8*10^{-11}$	m^2/s	[91]
α_a	Anodic rate transfer coefficients	0.5	-	[20]
α_c	Cathodic rate transfer coefficients	0.5	-	[20]
i_0	Exchange current density	3.45	mA/cm^3	measured
ρ_p	Density of ionic liquid	1.523	g/m^3	[92]
μ	Dynamic viscosity of ionic liquid	38.6	mPa·s	[92]
E	Equivalent bending modulus of CP	278	MPa	measured
M_s	Molar mass of ionic liquid	0.391	Kg/mol	[93]
β_{ss}	Coefficient of swelling	1.3e-5	m^3/kg	Fitting parameter
F	Faraday constant	96485	KJ	Constant
R	Gas constant	8.314	J.mol^{-1}.K^{-1}	Constant
T	Temperature	293.15	K	Constant

12. REFERENCES

1.   Bahramzadeh, Y.; Shahinpoor, M. A Review of Ionic Polymeric Soft Actuators and Sensors. *Soft Robot.* **2014**, *1*, 38–52.

2.   Smela, E.; Lnganas, O.; Lundstrom, L. Conducting polymers as artificial muscles: challenges and possibilities. *J. Micromech. Mbcroeng* **1993**, *3*, 203–205.

3.   Jager, E.W.; Smela, E.; Inganäs, O. Microfabricating conjugated polymer actuators. *Science* **2000**, *290*, 1540–5.

4.   Jager, E.W.H.; Smela, E.; Inganäs, O.; Lundström, I. Polypyrrole microactuators. *Synth. Met.* **1999**, *102*, 1309–1310.

5.   Chang, Y.C.; Kim, W.J. Aquatic ionic-polymer-metal-composite insectile robot with multi-DOF legs. *IEEE/ASME Trans. Mechatronics* **2013**, *18*, 547–555.

6.   Vunder, V. Modeling and characterization of back-relaxation of ionic electroactive polymer actuators, 2016.

7.   Mutlu, R.; Alici, G.; Li, W. A Soft Mechatronic Microstage Mechanism Based on Electroactive Polymer Actuators. *IEEE/ASME Trans. Mechatronics* **2016**, *21*, 1467–1478.

8.   Zhu, Z.; Asaka, K.; Chang, L.; Takagi, K.; Chen, H. Physical interpretation of deformation evolvement with water content of ionic polymer-metal composite actuator. *J. Appl. Phys.* **2013**, *114*, 184902.

9.   Simaite, A. Development of ionic electroactive actuators with improved interfacial adhesion: towards the fabrication of inkjet printable artificial muscles, Ph.D Thesis, University of Toulouse, 2015.

10.   Must, I.; Kaasik, F.; Põldsalu, I.; Mihkels, L.; Johanson, U.; Punning, A.; Aabloo, A. Ionic and capacitive artificial muscle for biomimetic soft robotics. *Adv. Eng. Mater.* **2015**, *17*, 84–94.

11.   Torop, J.; Palmre, V.; Arulepp, M.; Sugino, T.; Asaka, K.; Aabloo, A. Flexible supercapacitor-like actuator with carbide-derived carbon electrodes. *Carbon N. Y.* **2011**, *49*, 3113–3119.

12.   Temmer, R. Electrochemistry and novel applications of chemically synthesized conductive polymer electrodes, Ph.D Thesis, University of Tartu, 2014.

13.   Nuramdhani, I.; Gokceoren, A.T.; Odhiambo, S.A.; De Mey, G.D.; Hertleer, C.; Langenhove, L. Van Electrochemical impedance analysis of a PEDOT: PSS-based textile energy storage device. *Materials (Basel).* **2017**, *11*.

14.   Smela, E.; Inganas, O.; Lundstrom, I. Conducting polymers as artificial muscles: Challenges and possibilities. *J. Micromechanics Microengineering* **1993**, *3*, 203–205.

15.   Kim, S.-S.; Jeon, J.-H.; Kee, C.-D.; Oh, I.-K. Electro-active hybrid actuators based on freeze-dried bacterial cellulose and PEDOT:PSS. *Smart Mater. Struct.* **2013**, *22*, 085026.

16.   Pei, Q.; Inganäs, O. Electrochemical applications of the bending beam method. 1. Mass transport and volume changes in polypyrrole during redox. *J. Phys. Chem.* **1992**, *96*, 10507–10514.

17.   Punning, A.; Vunder, V.; Must, I.; Johanson, U.; Anbarjafari, G.; Aabloo, A. In situ scanning electron microscopy study of strains of ionic electroactive polymer actuators. *J. Intell. Mater. Syst. Struct.* **2016**, *27*, 1061–1074.

18. Shoa, T.; Yoo, D.S.; Walus, K.; Madden, J.D.W. A dynamic electromechanical model for electrochemically driven conducting polymer actuators. *IEEE/ASME Trans. Mechatronics* **2011**, *16*, 42–49.

19. Liu, Y.; Zhao, R.; Ghaffari, M.; Lin, J.; Liu, S.; Cebeci, H.; De Villoria, R.G.; Montazami, R.; Wang, D.; Wardle, B.L.; et al. Equivalent circuit modeling of ionomer and ionic polymer conductive network composite actuators containing ionic liquids. *Sensors Actuators, A Phys.* **2012**, *181*, 70–76.

20. Otero, T.F.; Martinez, J.G. Structural and biomimetic chemical kinetics: Kinetic magnitudes include structural information. *Adv. Funct. Mater.* **2013**, *23*, 404–416.

21. Martinez, J.G.; Otero, T.F. Biomimetic Dual Sensing-Actuators: Theoretical Description. Sensing Electrolyte Concentration and Driving Current. *J. Phys. Chem. B* **2012**, *116*, 9223–9230.

22. Alici, G.; Metz, P.; Spinks, G.M. A methodology towards geometry optimization of high performance polypyrrole (PPy) actuators. *Smart Mater. Struct.* **2006**, *15*, 243–252.

23. Metz, P.; Alici, G.; Spinks, G.M. A finite element model for bending behaviour of conducting polymer electromechanical actuators. *Sensors Actuators, A Phys.* **2006**, *130–131*, 1–11.

24. Stalbaum, T.; Pugal, D.; Nelson, S.E.; Palmre, V.; Kim, K.J. Physics-based modeling of mechano-electric transduction of tube-shaped ionic polymer-metal composite. *J. Appl. Phys.* **2015**, *117*, 114903.

25. Nemat-Nasser, S.; Li, J.Y. Electromechanical response of ionic polymer-metal composites. *J. Appl. Phys.* **2000**, *87*, 3321–3331.

26. Wallmersperger, T.; Leo, D.J.; Kothera, C.S. Transport modeling in ionomeric polymer transducers and its relationship to electromechanical coupling. *J. Appl. Phys.* **2007**, *101*, 024912.

27. Pugal, D.; Kim, K.J.; Aabloo, A. An explicit physics-based model of ionic polymer-metal composite actuators. *J. Appl. Phys.* **2011**, *110*, 084904.

28. Zhu, Z.; Chang, L.; Horiuchi, T.; Takagi, K.; Aabloo, A.; Asaka, K. Multi-physical model of cation and water transport in ionic polymer-metal composite sensors. *J. Appl. Phys.* **2016**, *119*, 124901.

29. Shen, Q.; Palmre, V.; Stalbaum, T.; Kim, K.J. A comprehensive physics-based model encompassing variable surface resistance and underlying physics of ionic polymer-metal composite actuators. *J. Appl. Phys.* **2015**, *118*, 124904.

30. Wallmersperger, T.; Leo, D.J.; Kothera, C.S. Transport modeling in ionomeric polymer transducers and its relationship to electromechanical coupling. *J. Appl. Phys.* **2007**, *101*, 024912.

31. Zhu, Z.; Asaka, K.; Chang, L.; Takagi, K.; Chen, H. Physical interpretation of deformation evolvement with water content of ionic polymer-metal composite actuator. *J. Appl. Phys.* **2013**, *114*, 184902.

32. Porfiri, M. An electromechanical model for sensing and actuation of ionic polymer metal composites. *Smart Mater. Struct.* **2008**, *18*, 015016.

33. Akle, B.J.; Wiles, K.B.; Leo, D.J.; McGrath, J.E. Effects of electrode morphology on the performance of BPSH and PATS ionic polymer transducers.; Bar-Cohen, Y., Ed.; International Society for Optics and Photonics, 2004; Vol. 5385, p. 413.

34. Chang, L.; Asaka, K.; Zhu, Z.; Wang, Y.; Chen, H.; Li, D. Effects of surface roughening on the mass transport and mechanical properties of ionic polymer-metal composite. *J. Appl. Phys.* **2014**, *115*, 244901.

35. Ebner, M.; Wood, V. Tool for Tortuosity Estimation in Lithium Ion Battery Porous Electrodes. *J. Electrochem. Soc.* **2015**, *162*, A3064–A3070.

36. Ott, J.; Völker, B.; Gan, Y.; McMeeking, R.M.; Kamlah, M. A micromechanical model for effective conductivity in granular electrode structures. *Acta Mech. Sin. Xuebao* **2013**, *29*, 682–698.

37. Smith, R.B.; Bazant, M.Z. Multiphase Porous Electrode Theory. *J. Electrochem. Soc.* **2017**, *164*, E3291–E3310.

38. Stalbaum, T.; Pugal, D.; Nelson, S.E.; Palmre, V.; Kim, K.J. Physics-based modeling of mechano-electric transduction of tube-shaped ionic polymer-metal composite. *J. Appl. Phys.* **2015**, *117*, 114903.

39. Horiuchi, T.; Kruusamäe, K.; Zhu, Z.; Asaka, K. Evaluating curvature and making picture-overlaid trajectory of motion of largely bent carbon nanotube composite bucky gel actuator using camera measurement system. *Sensors Actuators, A Phys.* **2015**, *235*, 28–36.

40. Verbrugge, M.W.; Liu, P. Microstructural Analysis and Mathematical Modeling of Electric Double-Layer Supercapacitors. *J. Electrochem. Soc.* **2005**, *152*, D79.

41. Brousse, T.; Bélanger, D.; Long, J.W. To Be or Not To Be Pseudocapacitive? *J. Electrochem. Soc.* **2015**, *162*, A5185–A5189.

42. Tevi, T.; Saint Birch, S.W.; Thomas, S.W.; Takshi, A. Effect of Triton X-100 on the double layer capacitance and conductivity of poly(3,4-ethylenedioxythiophene):poly(styrenesulfonate) (PEDOT:PSS) films. *Synth. Met.* **2014**, *191*, 59–65.

43. Ghosh, S.; Inganäs, O. Conducting Polymer Hydrogels as 3D Electrodes: Applications for Supercapacitors. *Adv. Mater.* **2002**, *11*, 1214–1218.

44. Volkov, A. V.; Wijeratne, K.; Mitraka, E.; Ail, U.; Zhao, D.; Tybrandt, K.; Andreasen, J.W.; Berggren, M.; Crispin, X.; Zozoulenko, I. V. Understanding the Capacitance of PEDOT:PSS. *Adv. Funct. Mater.* **2017**, *27*, 1700329.

45. Bard, A.J.; Faulkner, L.R. *Electrochemical methods : fundamentals and applications*; Wiley, 2001; ISBN 9780471043720.

46. Wang, W.; Wei, X.; Choi, D.; Lu, X.; Yang, G.; Sun, C. Electrochemical cells for medium- and large-scale energy storage: fundamentals. *Adv. Batter. Mediu. Large-Scale Energy Storage* **2015**, 3–28.

47. Newman, J.; Thomas-Alyea, K.E. *Electrochemical Systems*; J. Wiley, 2004; ISBN 0-471-47756-7.

48. Drummond, R.; Howey, D.A.; Duncan, S.R. Low-order mathematical modelling of electric double layer supercapacitors using spectral methods. *J. Power Sources* **2015**, *277*, 317–328.

49. Tavassol, H.; Jones, E.M.C.; Sottos, N.R.; Gewirth, A.A. Electrochemical stiffness in lithium-ion batteries. *Nat. Mater.* **2016**, *15*, 1182–1188.

50. Vunder, V.; Hamburg, E.; Punning, A.; Aabloo, A.; Johanson, U. Effect of ambient humidity on ionic electroactive polymer actuators. *Smart Mater. Struct.* **2016**, *25*, 055038.

51. Kaasik, F.; Must, I.; Baranova, I.; Põldsalu, I.; Lust, E.; Johanson, U.; Punning, A.; Aabloo, A. Scalable fabrication of ionic and capacitive laminate actuators for soft robotics. *Sensors Actuators B Chem.* **2017**, *246*, 154–163.

52. Akle, B.J.; Bennett, M.D.; Leo, D.J. High-strain ionomeric-ionic liquid electroactive actuators. *Sensors Actuators, A Phys.* **2006**, *126*, 173–181.

53. Wang, D.; Lu, C.; Zhao, J.; Han, S.; Wu, M.; Chen, W. High energy conversion efficiency conducting polymer actuators based on PEDOT:PSS/MWCNTs composite electrode. *RSC Adv.* **2017**, *7*, 31264–31271.

54. Kiefer, R.; Tamm, T.; Khorram, M.S.; Põldsalu, I.; Peikolainen, A.-L.; Rohtlaid, K.; Plesse, C.; Nguyen, T.M.G.; Vidal, F. Thin ink-jet printed trilayer actuators composed of PEDOT:PSS on interpenetrating polymer networks. *Sensors Actuators B Chem.* **2017**, *258*, 1072–1079.

55. Põldsalu, I.; Harjo, M.; Tamm, T.; Uibu, M.; Peikolainen, A.L.; Kiefer, R. Inkjet-printed hybrid conducting polymer-activated carbon aerogel linear actuators driven in an organic electrolyte. *Sensors Actuators, B Chem.* **2017**, *250*, 44–51.

56. Mallavarapu, K.; Newbury, K.M.; Leo, D.J. Feedback control of the bending response of ionic polymer-metal composite actuators. In Proceedings of the Smart Structures and Materials 2001: Electroactive Polymer Actuators and Devices; Bar-Cohen, Y., Ed.; International Society for Optics and Photonics, 2003; Vol. 4329, p. 301.

57. Bergaud, C.; Tondu, B.; Souères, P.; Mesnilgrente, F.; Simaite, A. Towards inkjet printable conducting polymer artificial muscles. *Sensors Actuators B Chem.* **2016**, *229*, 425–433.

58. Otero, T.F. Reactive conducting polymers as actuating sensors and tactile muscles. *Bioinspiration and Biomimetics* **2008**, *3*, 035004.

59. Jager, E.W.H.; Masurkar, N.; Nworah, N.F.; Gaihre, B.; Alici, G.; Spinks, G.M. Patterning and electrical interfacing of individually controllable conducting polymer microactuators. *Sensors Actuators, B Chem.* **2013**, *183*, 283–289.

60. Põldsalu, I.; Mändmaa, S.-E.; Peikolainen, A.-L.; Kesküla, A.; Aabloo, A. Fabrication of ion-conducting carbon-polymer composite electrodes by spin-coating. In Proceedings of the Electroactive Polymer Actuators and Devices (EAPAD) 2015; Bar-Cohen, Y., Ed.; 2015; Vol. 9430, p. 943019.

61. Simaite, A.; Bergaud, C.; Tondu, B.; Souéres, P.; Mathieu, F. Simple casting based fabrication of PEDOT:PSS-PVDF-ionic liquid soft actuators. In Proceedings of the Electroactive Polymer Actuators and Devices (EAPAD) 2015; Bar-Cohen, Y., Ed.; International Society for Optics and Photonics, 2015; Vol. 9430, p. 94301E.

62. Saarinen, J.J.; Toivakka, M.; Liu, J.; Kumar, V.; Xu, C.; Valtakari, D. Conductivity of PEDOT:PSS on Spin-Coated and Drop Cast Nanofibrillar Cellulose Thin Films. *Nanoscale Res. Lett.* **2015**, *10*, 386.

63. Maziz, A.; Plesse, C.; Soyer, C.; Chevrot, C.; Teyssié, D.; Cattan, E.; Vidal, F. Demonstrating kHz frequency actuation for conducting polymer microactuators. *Adv. Funct. Mater.* **2014**, *24*, 4851–4859.

64. Khaldi, A.; Falk, D.; Bengtsson, K.; Maziz, A.; Filippini, D.; Robinson, N.D.; Jager, E.W.H. Patterning Highly Conducting Conjugated Polymer Electrodes for Soft and Flexible Microelectrochemical Devices. *ACS Appl. Mater. Interfaces* **2018**, *10*, 14978–14985.

65. Derby, B. Inkjet Printing of Functional and Structural Materials: Fluid Property Requirements, Feature Stability, and Resolution. *Annu. Rev. Mater. Res.* **2010**, *40*, 395–414.

66.   De Gans, B.J.; Duineveld, P.C.; Schubert, U.S. Inkjet printing of polymers: State of the art and future developments. *Adv. Mater.* 2004, *16*, 203–213.

67.   Pranzo, D.; Larizza, P.; Filippini, D.; Percoco, G. Extrusion-Based 3D Printing of Microfluidic Devices for Chemical and Biomedical Applications: A Topical Review. *Micromachines* **2018**, *9*, 374.

68.   Yun, H.U.; Kim, C.J.; Kim, S.J.; Park, N.C.; Yang, H.; Park, Y.-P. Design of micromirror actuator by ionic polymer metal composites. *Microsyst. Technol.* **2009**, *15*, 1531–1538.

69.   Tsai, S.-A.; Wei, H.-C.; Su, G.-D.J. Polydimethylsiloxane coating on an ionic polymer metallic composite for a tunable focusing mirror. *Appl. Opt.* **2012**, *51*, 8315.

70.   Chen, W.-H.; Lu, J.-S.; Su, G.-D.J. Ionic polymer metal composite for an optical zoom in a compact camera. *Opt. Express* **2015**, *23*, 13265.

71.   Yamakita, M.; Kamamichi, N.; Kaneda, Y.; Asaka, K.; Luo, Z.-W. Development of an artificial muscle linear actuator using ionic polymer–metal composites. *Adv. Robot.* **2004**, *18*, 383–399.

72.   Torop, J.; Arulepp, M.; Leis, J.; Punning, A.; Johanson, U.; Palmre, V.; Aabloo, A. Nanoporous carbide-derived carbon material-based linear actuators. *Materials (Basel).* **2010**, *3*, 9–25.

73.   Campbell, R.A.A.; Eifert, R.W.; Turner, G.C. Openstage: A low-cost motorized microscope stage with sub-micron positioning accuracy. *PLoS One* **2014**, *9*, e88977.

74.   Newbury, K. Characterization , Modeling , and Control of Ionic Polymer Transducers by Characterization , Modeling , and Control of Ionic Polymer Transducers. *Mech. Eng.* **2002**.

75.   Yang Fang; Xiaobo Tan; Alici, G. Robust Adaptive Control of Conjugated Polymer Actuators. *IEEE Trans. Control Syst. Technol.* **2008**, *16*, 600–612.

76.   Ljung, L. Prediction error estimation methods. *Circuits, Syst. Signal Process.* **2002**, *21*, 11–21.

77.   Ljung, L. System Identification. In; Birkhäuser, Boston, MA, 1998; pp. 163–173.

78.   Ruth, D.J.S.; Dhanalakshmi, K.; Nakshatharan, S.S. Interrogation of Undersensing for an Underactuated Dynamical System. *IEEE Sens. J.* **2015**, *15*, 2203–2211.

79.   Nguyen, K.T.; Ko, S.Y.; Park, J.O.; Park, S. Terrestrial Walking Robot with 2DoF Ionic Polymer-Metal Composite (IPMC) Legs. *IEEE/ASME Trans. Mechatronics* **2015**, *20*, 2962–2972.

80.   Hao, L.; Chen, Y.; Sun, Z. The sliding mode control for different shapes and dimensions of IPMC on resisting its creep characteristics. *Smart Mater. Struct.* **2015**, *24*, 045040.

81.   Brufau-Penella, J.; Tsiakmakis, K.; Laopoulos, T.; Puig-Vidal, M. Model reference adaptive control for an ionic polymer metal composite in underwater applications. *Smart Mater. Struct.* **2008**, *17*, 045020.

82.   Liuping Wang Model Predictive Control: Design and implementation using MATLAB (T-3). In Proceedings of the 2009 American Control Conference; IEEE, 2009; pp. 25–26.

83.   Mohanty, S. Artificial neural network based system identification and model predictive control of a flotation column. *J. Process Control* **2009**, *19*, 991–999.

84.   Discrete-time MPC for beginners. In *Advances in Industrial Control*; Springer London: London, 2009; pp. 1–42.

85.   Honc, D.; Sharma K., R.; Abraham, A.; Dušek, F.; Pappa, N. Teaching and Practicing Model Predictive Control. *IFAC-PapersOnLine* **2016**, *49*, 34–39.

86.   Barlas, T.K.; van der Veen, G.J.; van Kuik, G.A.M. Model predictive control for wind turbines with distributed active flaps: incorporating inflow signals and actuator constraints. *Wind Energy* **2012**, *15*, 757–771.

87.   Torop, J. Carbide-derived carbon-based electromechanical actuators, Ph.D Thesis, University of Tartu, 2012.

88.   Wong, C.L.; Soriano, A.N.; Li, M.H. Diffusion coefficients and molar conductivities in aqueous solutions of 1-ethyl-3-methylimidazolium-based ionic liquids. *Fluid Phase Equilib.* **2008**, *271*, 43–52.

89.   1-Ethyl-3-methylimidazolium trifluoromethanesulfonate ≥98.0% (T) | Sigma-Aldrich Available online:
        https://www.sigmaaldrich.com/catalog/product/sial/04367?lang=en&region=IN (accessed on Jul 26, 2018).

90.   Freire, M.G.; Teles, A.R.R.; Rocha, M.A.A.; Schröder, B.; Neves, C.M.S.S.; Carvalho, P.J.; Evtuguin, D. V.; Santos, L.M.N.B.F.; Coutinho, J.A.P. Thermophysical characterization of ionic liquids able to dissolve biomass. *J. Chem. Eng. Data* **2011**, *56*, 4813–4822.

91.   Gouverneur, M.; Kopp, J.; Van Wüllen, L.; Schönhoff, M. Direct determination of ionic transference numbers in ionic liquids by electrophoretic NMR. *Phys. Chem. Chem. Phys.* **2015**, *17*, 30680–30686.

92.   Fröba, A.P.; Kremer, H.; Leipertz, A. Density, Refractive Index, Interfacial Tension, and Viscosity of Ionic Liquids [EMIM][EtSO$_4$], [EMIM][NTf$_2$], [EMIM][N(CN)$_2$], and [OMA][NTf$_2$] in Dependence on Temperature at Atmospheric Pressure. *J. Phys. Chem. B* **2008**, *112*, 12420–12430.

93.   Product Im0208a / 1-Ethyl-3-methylimidazolium bis(trifluoromethanesulfonyl)imide 99.9% Available online:
        http://en.solvionic.com/products/1-ethyl-3-methylimidazolium-bistrifluoromethanesulfonylimide-99.9 (accessed on Feb 22, 2019).

13. ACKNOWLEDGEMENTS

First I would like to thank my supervisors Prof. Alvo Aabloo and Dr. Andres Punning for giving me this wonderful opportunity to do research in IMS lab and to explore the small but beautiful Estonia. I express my sincere gratitude to both my supervisor for providing guidance and complete support throughout this study. My special thanks to Dr. Urmas Johanson for the continued support during the study in performing experiments and providing invaluable knowledge in the field of electrochemistry. I am grateful to all my friends and supportive colleagues of IMS Lab who have helped me to reach my goals and would like to thank Mariana Kukk for supporting all administrative duties and also finding accommodation and thank Pille Rinne for proofreading this thesis.

I would like to acknowledge Prof. Hyacinthe Randriamahazaka, Université Paris Diderot, Paris, France and Dr. Edwin W.H. Jager, Division of Sensor and Actuator Systems, Linköping, Sweden for supporting and hosting me during the visit to their respective institutes.

Last, but not least, I very much appreciate the continuous support from my mother and sister, and friends back in India.

Thank you all, for making this journey special!

PUBLICATIONS

CURRICULUM VITAE

Name: S. Sunjai Nakshatharan
Date of birth: August 1, 1987
Citizenship: India
E-mail: sunjainakshatharan@gmail.com

Education
2015–   University of Tartu, Faculty of Science and Technology, Ph.D. Student
2011–2014   National Institute of Technology-Tiruchirappalli, India, Instrumentation and Control Engineering, Master of Science (by Research)
2005–2009   Anna University, Chennai, India, Electrical and Electronics Engineering, Bachelor of Engineering,

Work experience
2015–2018   Estrotech OÜ, Marie Sklodowska-Curie grant No 641822, Early Stage Researcher
2018   Linkoping University, Sweden, Biosensors & Bioelectronics Centre, Dept. of Physics, Chemistry and Biology (IFM), Visiting Researcher
2016–2017   University of Paris Diderot, France, NanoElectroChemistry Group, ITODYS CNRS – UMR, Visiting Researcher
2014–2015   Continental Automotive Systems, Bangalore, India. Research Intern
2009–2010   JPR Engineering Industry, Coimbatore, India, Electrical Engineer

Publications:

1.1. Scholarly articles indexed by Thompson Reuters Web of Science:

- A. Epljakov, V. Vunder, E. Petlenkov, S. Nakshatharan, A. Punning, V. Kaparin, J. Belikov, A. Aabloo, "Fractional-order Modeling and Control of Ionic Polymer-Metal Composite Actuator" *Smart Materials and Structures* (Accepted)

- S. Nakshatharan, U. Johanson, A. Punning and A. Aabloo, "Effect of porosity and tortuosity of electrodes on carbon polymer soft actuators," Journal of Applied Physics, 123, 014502, 2018.

- S. Nakshatharan, U. Johanson, A. Punning and A. Aabloo, "Modeling, Fabrication, and Characterization of Motion Platform Actuated by Carbon Polymer Soft Actuator" Sensors and Actuators A: Physical, 283, 87–97, 2018.

- S. Nakshatharan, V. Vunder, I. Põldsalu, U. Johanson, A. Punning and A. Aabloo, "Modelling and control of ionic electroactive polymer actuators under varying humidity conditions," Actuators, 7(1), 7–20, 2018

- Z. Zondaka, A. Kivilo, S. Nakshatharan, K. A. Küppar, U. Johanson, T. Tamm, R. Kiefer, "Carbide-derived carbon and poly-3,4-ethylenedioxythiphene composite trilayer: linear and bending actuation," *Synthetic Metals*, 245, 67–73, 2018.

- S. Nakshatharan, A. Punning and A. Aabloo,, "A Neural Network Modelling and Sliding Mode Control of Self Sensing IPMC Actuator" *Journal of Intelligent Materials Systems and Structures,* Vol 28, Issue 20, 3163–3174, 2017.

- S. Nakshatharan, D.J.S Ruth and K Dhanalakshmi, "Experimental study on effect of stress over bandwidth in antagonistic shape memory alloy from control perspective", *Journal of Intelligent Material Systems and Structures,* Vol 27, Issue 2, pp. 153–165, 2016.

- S. Nakshatharan, K Dhanalakshmi and D.J.S Ruth, "Fuzzy-based sliding surface for shape memory alloy wire actuated classical super-articulated control system", *Applied Soft Computing*, 32, 580–589, 2015.

- D.J.S Ruth, K. Dhanalakshmi and S. Nakshatharan, "Interrogation of undersensing an under-actuated dynamical system", *IEEE Sensors Journal*, vol. 15, no. 4, pp. 2203–2211, 2015.

- D.J.S Ruth, K. Dhanalakshmi and S. Nakshatharan, 2015 "Bidirectional angular control of an integrated sensor/actuator shape memory alloy based system " *Measurement,* 69, 210–221, 2015.

- S. Nakshatharan, D.J.S Ruth and K Dhanalakshmi, "Servo control of an under actuated system using antagonistic shape memory alloy", *Smart Structures and Systems*, 14(4), 643–658, 2014.

- S. Nakshatharan, D.J.S Ruth and K Dhanalakshmi, "Dynamic stabilization and rapid motion control system driven by antagonistic shape memory alloy actuators", *Journal of Vibration and Control*, Vol 21, Issue 16, pp. 3189 – 3204, 2014

- D.J.S Ruth, S. Nakshatharan and K. Dhanalakshmi, 2014 "Differential resistance feedback control of a self-sensing shape memory alloy actuated system", *ISA Transactions,* 53 (2), pp. 289–297, 2014.
- D.J.S Ruth, S. Nakshatharan and K. Dhanalakshmi, 2013 "Auto adaptive control of one joint arm direct driven by antagonistic shape memory alloy" *International Journal of Smart Sensing and Intelligent Systems*, 6(3), 833–849, 2013.

3.1. Articles in collections indexed by the Thompson Reuters Conference Proceedings Citation Index:

- S. Nakshatharan, U. Johanson, A. Punning and A. Aabloo, , "Modelling and control of self-sensing ionic electroactive polymer actuator", *Proc. SPIE 10966, Electroactive Polymer Actuators and Devices (EAPAD) XXI, 109661C,* 2019.
- S. Nakshatharan, U. Johanson, A. Punning and A. Aabloo, "Fabrication of Carbon Polymer Composite Manipulated Multi Degree Motion Platform", *Proc. SPIE 10594, Electroactive Polymer Actuators and Devices (EAPAD) XX, 105941Y,* 2018.
- A. Kivilo, Z. Zondaka, S. Nakshatharan, K.A. Küppar, T. Tamm, R. Kiefer "Poly-3,4-ethylenedixoythiophene on carbide-derived carbon trilayer: combined linear actuation characterization" *Proc. SPIE 10594, Electroactive Polymer Actuators and Devices (EAPAD) XX, 105942L,* 2018.
- S. Nakshatharan, U. Johanson, A. Punning and A. Aabloo, "Effect of porosity of the electrodes on ionic electroactive polymer actuators" *Proc. SPIE 10163, Electroactive Polymer Actuators and Devices (EAPAD), 101632I,* 2017.
- S. Nakshatharan, A. Punning and A. Aabloo, "Temperature and humidity dependence of ionic electroactive polymer actuators" *Proc. SPIE 10163, Electroactive Polymer Actuators and Devices (EAPAD), 1016313,* 2017.
- S. Nakshatharan, U. Johanson, A. Punning and A. Aabloo, "Effect of electrical terminals made of copper to the ionic electroactive polymer actuators" *Proc. SPIE 10163, Electroactive Polymer Actuators and Devices (EAPAD), 101632M,* 2017.
- S. Nakshatharan, A. Punning, S. Assi, U. Johanson, A. Aabloo, "Fish-skeleton visualization of bending actuators" *Proc. SPIE 9798, Electroactive Polymer Actuators and Devices (EAPAD), Las Vegas, USA.* 2016, 97981P
- S. Nakshatharan, A. Punning and A. Aabloo, "Neural network modeling and model predictive control of ionic electroactive polymer actuators" *Proc. SPIE 9798, Electroactive Polymer Actuators and Devices (EAPAD), Las Vegas, USA.* 2016, 97982J
- S. Nakshatharan, D.J.S Ruth and K Dhanalakshmi, "Design and experimental evaluation of higher order sliding mode control for vibration suppression of shape memory alloy actuated structure", *Proc. International Confe-*

rence on Advances in Control and Optimization of Dynamical Systems, March 2014, India.

- D.J.S Ruth, S. Nakshatharan and K. Dhanalakshmi, "Prospective self-sensing actuator for stabilised control: beam balancing ball driven by shape memory alloy", *Proc. of International Conference on Advances in Control and Optimization of Dynamical Systems,* March 2014, India.

- D.J.S Ruth, S. Nakshatharan and K. Dhanalakshmi, "Auto-sensing Antagonistic Shape Memory Alloy Wire Actuated Manipulator", *Proc. IEEE Multi-Conference on Systems and Control*, August 2013, India.

- M. BanuSundareswari, K. Dhanalakshmi, S. Nakshatharan and D.J.S Ruth, "Optimal design of PID controller for SMA actuated ball on beam system", *Proc. International Conference on Intelligent Unmanned Systems*, September 2013, India.

- S. Nakshatharan, D.J.S Ruth and K Dhanalakshmi, "*Design based Active Vibration Control of a Flexible Structure using Shape Memory Alloy Wire Actuators*", *Proc. IEEE International Conference on Sensing Technology*, December 2012, India

- D.J.S Ruth, S. Nakshatharan and K. Dhanalakshmi, "*Angular Trajectory Tracking using Antagonistic Shape Memory Alloy Actuators*", *Proc. IEEE International Conference on Sensing Technology*, December 2012. India.

- S. Nakshatharan, K Dhanalakshmi and D.J.S Ruth, "A new ball and beam system using shape memory alloy actuators", *Proc. Third Asian Conference on Mechanics of Functional Materials and Structures*, December 2012, India.

- D.J.S Ruth, K. Dhanalakshmi and S. Nakshatharan, "Force Measurement using Self-Sensing Shape Memory Alloy", *Proc. Third Asian Conference on Mechanics of Functional Materials and Structures*, December 2012, India.

ELULOOKIRJELDUS

Nimi: S. Sunjai Nakshatharan
Sünniaeg: 1. august 1987
Kodakondsus: India
E-mail: sunjainakshatharan@gmail.com

Haridustee

2015–	Tartu Ülikool, Loodus- ja Tehnoloogiateaduskond, tehnika ja tehnoloogia doktoriõpe
2011–2014	Tiruchirappalli Riiklik Tehnoloogiainstituut, India, süsteemide ja kontrolli insenerteaduse magister (by Research)
2005–2009	Anna Ülikool, Chennai, India, elektri ja elektroonika alase inseneriteaduse bakalaureus

Teenistuskäik

2015 –2018	Estrotech OÜ, Marie Sklodowska-Curie grant No 641822, nooremteadur
2018	Linköpingi Ülikool, Biosensorite ja bioelektroonika keskus, Füüsika, keemia ja bioloogia osakond, Rootsi, külalisteadlane
2016–2017	Paris Diderot Ülikool, NanoElektroKeemia grupp, ITODYS CNRS – UMR, Prantsusmaa, külalisteadlane
2014–2015	Continental Automotive Systems, Bangalore, India, intern
2009–2010	JPR Engineering Industry, Coimbatore, India, elektriinsener

Publikatsioonid:

Thompson Reuters Web of Science andmebaasis kajastatud 1.1 teadusartiklid:

- A. Epljakov, V. Vunder, E. Petlenkov, S. Nakshatharan, A. Punning, V. Kaparin, J. Belikov, A. Aabloo, "Fractional-order Modeling and Control of Ionic Polymer-Metal Composite Actuator" *Smart Materials and Structures* (Accepted)

- S. Nakshatharan, U. Johanson, A. Punning and A. Aabloo, "Effect of porosity and tortuosity of electrodes on carbon polymer soft actuators," *Journal of Applied Physics*, 123, 014502, 2018.

- S. Nakshatharan, U. Johanson, A. Punning and A. Aabloo, "Modeling, Fabrication, and Characterization of Motion Platform Actuated by Carbon Polymer Soft Actuator" *Sensors and Actuators A: Physical*, 283, 87–97, 2018.

- S. Nakshatharan, V. Vunder, I. Põldsalu, U. Johanson, A. Punning and A. Aabloo, "Modelling and control of ionic electroactive polymer actuators under varying humidity conditions," *Actuators*, 7(1), 7–20, 2018

- Z. Zondaka, A. Kivilo, S. Nakshatharan, K. A. Küppar, U. Johanson, T. Tamm, R. Kiefer, "Carbide-derived carbon and poly-3,4-ethylenedioxythiphene composite trilayer: linear and bending actuation," *Synthetic Metals*, 245, 67–73, 2018.

- S. Nakshatharan, A. Punning and A. Aabloo,, "A Neural Network Modelling and Sliding Mode Control of Self Sensing IPMC Actuator" *Journal of Intelligent Materials Systems and Structures,* Vol 28, Issue 20, 3163–3174, 2017.

- S. Nakshatharan, D.J.S Ruth and K Dhanalakshmi, "Experimental study on effect of stress over bandwidth in antagonistic shape memory alloy from control perspective", *Journal of Intelligent Material Systems and Structures,* Vol 27, Issue 2, pp. 153–165, 2016.

- S. Nakshatharan, K Dhanalakshmi and D.J.S Ruth, "Fuzzy-based sliding surface for shape memory alloy wire actuated classical super-articulated control system", *Applied Soft Computing*, 32, 580–589, 2015.

- D.J.S Ruth, K. Dhanalakshmi and S. Nakshatharan, "Interrogation of undersensing an under-actuated dynamical system", *IEEE Sensors Journal*, vol. 15, no. 4, pp. 2203–2211, 2015.

- D.J.S Ruth, K. Dhanalakshmi and S. Nakshatharan, 2015 "Bidirectional angular control of an integrated sensor/actuator shape memory alloy based system " *Measurement,* 69, 210- 221, 2015.

- S. Nakshatharan, D.J.S Ruth and K Dhanalakshmi, "Servo control of an under actuated system using antagonistic shape memory alloy", *Smart Structures and Systems*, 14(4), 643–658, 2014.

- S. Nakshatharan, D.J.S Ruth and K Dhanalakshmi, "Dynamic stabilization and rapid motion control system driven by antagonistic shape memory alloy actuators", *Journal of Vibration and Control*, Vol 21, Issue 16, pp. 3189–3204, 2014

- D.J.S Ruth, S. Nakshatharan and K. Dhanalakshmi, 2014 "Differential resistance feedback control of a self-sensing shape memory alloy actuated system", *ISA Transactions,* 53 (2), pp. 289–297,2014.
- D.J.S Ruth, S. Nakshatharan and K. Dhanalakshmi, 2013 "Auto adaptive control of one joint arm direct driven by antagonistic shape memory alloy" *International Journal of Smart Sensing and Intelligent Systems*, 6(3), 833–849, 2013.

3.1 artiklid Thompson Reuters Conference Proceedings Citation Index poolt refereeritud kogumikus:

- S. Nakshatharan, U. Johanson, A. Punning and A. Aabloo, , "Modelling and control of self-sensing ionic electroactive polymer actuator", *Proc. SPIE 10966, Electroactive Polymer Actuators and Devices (EAPAD) XXI, 109661C,* 2019.
- S. Nakshatharan, U. Johanson, A. Punning and A. Aabloo, "Fabrication of Carbon Polymer Composite Manipulated Multi Degree Motion Platform", *Proc. SPIE 10594, Electroactive Polymer Actuators and Devices (EAPAD) XX, 105941Y,* 2018.
- A. Kivilo, Z. Zondaka, S. Nakshatharan, K.A. Küppar, T. Tamm, R. Kiefer "Poly-3,4-ethylenedixoythiophene on carbide-derived carbon trilayer: combined linear actuation characterization" *Proc. SPIE 10594, Electroactive Polymer Actuators and Devices (EAPAD) XX, 105942L,* 2018.
- S. Nakshatharan, U. Johanson, A. Punning and A. Aabloo, "Effect of porosity of the electrodes on ionic electroactive polymer actuators" *Proc. SPIE 10163, Electroactive Polymer Actuators and Devices (EAPAD), 101632I,* 2017.
- S. Nakshatharan, A. Punning and A. Aabloo, "Temperature and humidity dependence of ionic electroactive polymer actuators" *Proc. SPIE 10163, Electroactive Polymer Actuators and Devices (EAPAD), 1016313,* 2017.
- S. Nakshatharan, U. Johanson, A. Punning and A. Aabloo, "Effect of electrical terminals made of copper to the ionic electroactive polymer actuators" *Proc. SPIE 10163, Electroactive Polymer Actuators and Devices (EAPAD), 101632M,* 2017.
- S. Nakshatharan, A. Punning, S. Assi, U. Johanson, A. Aabloo, "Fish-skeleton visualization of bending actuators" *Proc. SPIE 9798, Electroactive Polymer Actuators and Devices (EAPAD), Las Vegas, USA.* 2016, 97981P
- S. Nakshatharan, A. Punning and A. Aabloo, "Neural network modeling and model predictive control of ionic electroactive polymer actuators" *Proc. SPIE 9798, Electroactive Polymer Actuators and Devices (EAPAD), Las Vegas, USA.* 2016, 97982J
- S. Nakshatharan, D.J.S Ruth and K Dhanalakshmi, "Design and experimental evaluation of higher order sliding mode control for vibration suppression of shape memory alloy actuated structure", *Proc. International*

Conference on Advances in Control and Optimization of Dynamical Systems, March 2014, India.

- D.J.S Ruth, S. Nakshatharan and K. Dhanalakshmi, "Prospective self-sensing actuator for stabilised control: beam balancing ball driven by shape memory alloy", *Proc. of International Conference on Advances in Control and Optimization of Dynamical Systems,* March 2014, India.

- D.J.S Ruth, S. Nakshatharan and K. Dhanalakshmi, "Auto-sensing Antagonistic Shape Memory Alloy Wire Actuated Manipulator", *Proc. IEEE Multi-Conference on Systems and Control*, August 2013, India.

- M. BanuSundareswari, K. Dhanalakshmi, S. Nakshatharan and D.J.S Ruth, "Optimal design of PID controller for SMA actuated ball on beam system", *Proc. International Conference on Intelligent Unmanned Systems*, September 2013, India.

- S. Nakshatharan, D.J.S Ruth and K Dhanalakshmi, "*Design based Active Vibration Control of a Flexible Structure using Shape Memory Alloy Wire Actuators*", *Proc. IEEE International Conference on Sensing Technology*, December 2012, India

- D.J.S Ruth, S. Nakshatharan and K. Dhanalakshmi, "*Angular Trajectory Tracking using Antagonistic Shape Memory Alloy Actuators*", *Proc. IEEE International Conference on Sensing Technology*, December 2012. India.

- S. Nakshatharan, K Dhanalakshmi and D.J.S Ruth, "A new ball and beam system using shape memory alloy actuators", *Proc. Third Asian Conference on Mechanics of Functional Materials and Structures*, December 2012, India.

- D.J.S Ruth, K. Dhanalakshmi and S. Nakshatharan, "Force Measurement using Self-Sensing Shape Memory Alloy", *Proc. Third Asian Conference on Mechanics of Functional Materials and Structures*, December 2012, India.

DISSERTATIONES TECHNOLOGIAE
UNIVERSITATIS TARTUENSIS

1. **Imre Mäger**. Characterization of cell-penetrating peptides: Assessment of cellular internalization kinetics, mechanisms and bioactivity. Tartu 2011, 132 p.
2. **Taavi Lehto**. Delivery of nucleic acids by cell-penetrating peptides: application in modulation of gene expression. Tartu 2011, 155 p.
3. **Hannes Luidalepp**. Studies on the antibiotic susceptibility of *Escherichia coli*. Tartu 2012, 111 p.
4. **Vahur Zadin**. Modelling the 3D-microbattery. Tartu 2012, 149 p.
5. **Janno Torop**. Carbide-derived carbon-based electromechanical actuators. Tartu 2012, 113 p.
6. **Julia Suhorutšenko**. Cell-penetrating peptides: cytotoxicity, immunogenicity and application for tumor targeting. Tartu 2012, 139 p.
7. **Viktoryia Shyp**. G nucleotide regulation of translational GTPases and the stringent response factor RelA. Tartu 2012, 105 p.
8. **Mardo Kõivomägi**. Studies on the substrate specificity and multisite phosphorylation mechanisms of cyclin-dependent kinase Cdk1 in *Saccharomyces cerevisiae*. Tartu, 2013, 157 p.
9. **Liis Karo-Astover**. Studies on the Semliki Forest virus replicase protein nsP1. Tartu, 2013, 113 p.
10. **Piret Arukuusk**. NickFects–novel cell-penetrating peptides. Design and uptake mechanism. Tartu, 2013, 124 p.
11. **Piret Villo**. Synthesis of acetogenin analogues. Asymmetric transfer hydrogenation coupled with dynamic kinetic resolution of α-amido-β-keto esters. Tartu, 2013, 151 p.
12. **Villu Kasari**. Bacterial toxin-antitoxin systems: transcriptional cross-activation and characterization of a novel *mqsRA* system. Tartu, 2013, 108 p.
13. **Margus Varjak**. Functional analysis of viral and host components of alphavirus replicase complexes. Tartu, 2013, 151 p.
14. **Liane Viru**. Development and analysis of novel alphavirus-based multi-functional gene therapy and expression systems. Tartu, 2013, 113 p.
15. **Kent Langel**. Cell-penetrating peptide mechanism studies: from peptides to cargo delivery. Tartu, 2014, 115 p.
16. **Rauno Temmer**. Electrochemistry and novel applications of chemically synthesized conductive polymer electrodes. Tartu, 2014, 206 p.
17. **Indrek Must**. Ionic and capacitive electroactive laminates with carbonaceous electrodes as sensors and energy harvesters. Tartu, 2014, 133 p.
18. **Veiko Voolaid**. Aquatic environment: primary reservoir, link, or sink of antibiotic resistance? Tartu, 2014, 79 p.
19. **Kristiina Laanemets**. The role of SLAC1 anion channel and its upstream regulators in stomatal opening and closure of *Arabidopsis thaliana*. Tartu, 2015, 115 p.

20. **Kalle Pärn**. Studies on inducible alphavirus-based antitumour strategy mediated by site-specific delivery with activatable cell-penetrating peptides. Tartu, 2015, 139 p.
21. **Anastasia Selyutina**. When biologist meets chemist: a search for HIV-1 inhibitors. Tartu, 2015, 172 p.
22. **Sirle Saul**. Towards understanding the neurovirulence of Semliki Forest virus. Tartu, 2015, 136 p.
23. **Marit Orav**. Study of the initial amplification of the human papillomavirus genome. Tartu, 2015, 132 p.
24. **Tormi Reinson**. Studies on the Genome Replication of Human Papillomaviruses. Tartu, 2016, 110 p.
25. **Mart Ustav Jr**. Molecular Studies of HPV-18 Genome Segregation and Stable Replication. Tartu, 2016, 152 p.
26. **Margit Mutso**. Different Approaches to Counteracting Hepatitis C Virus and Chikungunya Virus Infections. Tartu, 2016, 184 p.
27. **Jelizaveta Geimanen**. Study of the Papillomavirus Genome Replication and Segregation. Tartu, 2016, 168 p.
28. **Mart Toots**. Novel Means to Target Human Papillomavirus Infection. Tartu, 2016, 173 p.
29. **Kadi-Liis Veiman**. Development of cell-penetrating peptides for gene delivery: from transfection in cell cultures to induction of gene expression *in vivo*. Tartu, 2016, 136 p.
30. **Ly Pärnaste**. How, why, what and where: Mechanisms behind CPP/cargo nanocomplexes. Tartu, 2016, 147 p.
31. **Age Utt**. Role of alphavirus replicase in viral RNA synthesis, virus-induced cytotoxicity and recognition of viral infections in host cells. Tartu, 2016, 183 p.
32. **Veiko Vunder**. Modeling and characterization of back-relaxation of ionic electroactive polymer actuators. Tartu, 2016, 154 p.
33. **Piia Kivipõld**. Studies on the Role of Papillomavirus E2 Proteins in Virus DNA Replication. Tartu, 2016, 118 p.
34. **Liina Jakobson**. The roles of abscisic acid, CO_2, and the cuticle in the regulation of plant transpiration. Tartu, 2017, 162 p.
35. **Helen Isok-Paas**. Viral-host interactions in the life cycle of human papillomaviruses. Tartu, 2017, 158 p.
36. **Hanna Hõrak**. Identification of key regulators of stomatal CO_2 signalling via O_3-sensitivity. Tartu, 2017, 260 p.
37. **Jekaterina Jevtuševskaja**. Application of isothermal amplification methods for detection of *Chlamydia trachomatis* directly from biological samples. Tartu, 2017, 96 p.
38. **Ülar Allas.** Ribosome-targeting antibiotics and mechanisms of antibiotic resistance. Tartu, 2017, 152 p.
39. **Anton Paier.** Ribosome Degradation in Living Bacteria. Tartu, 2017, 108 p.
40. **Vallo Varik.** Stringent Response in Bacterial Growth and Survival. Tartu, 2017, 101 p.

41. **Pavel Kudrin.** In search for the inhibitors of *Escherichia coli* stringent response factor RelA. Tartu, 2017, 138 p.
42. **Liisi Henno.** Study of the human papillomavirus genome replication and oligomer generation. Tartu, 2017, 144 p.
43. **Katrin Krõlov.** Nucleic acid amplification from crude clinical samples exemplified by *Chlamydia trachomatis* detection in urine. Tartu, 2018, 118 p.
44. **Eve Sankovski.** Studies on papillomavirus transcription and regulatory protein E2. Tartu, 2018, 113 p.
45. **Morteza Daneshmand.** Realistic 3D Virtual Fitting Room. Tartu, 2018, 233 p.
46. **Fatemeh Noroozi.** Multimodal Emotion Recognition Based Human-Robot Interaction Enhancement. Tartu, 2018, 113 p.
47. **Krista Freimann.** Design of peptide-based vector for nucleic acid delivery in vivo. Tartu, 2018, 103 p.
48. **Rainis Venta.** Studies on signal processing by multisite phosphorylation pathways of the *S. cerevisiae* cyclin-dependent kinase inhibitor Sic1. Tartu, 2018, 155 p.
49. **Inga Põldsalu.** Soft actuators with ink-jet printed electrodes. Tartu, 2018, 85 p.
50. **Kadri Künnapuu**. Modification of the cell-penetrating peptide PepFect14 for targeted tumor gene delivery and reduced toxicity. Tartu, 2018, 114 p.
51. **Toomas Mets**. RNA fragmentation by MazF and MqsR toxins of *Escherichia coli.* Tartu, 2019, 119 p.
52. **Kadri Tõldsepp**. The role of mitogen-activated protein kinases MPK4 and MPK12 in CO_2-induced stomatal movements. Tartu, 2019, 259 p.
53. **Pirko Jalakas**. Unravelling signalling pathways contributing to stomatal conductance and responsiveness. Tartu, 2019, 120 p.